DISCRETE NUMERICAL SIMULATIONS OF SOLID OXIDE FUEL CELL ELECTRODES DEVELOPING NEW TOOLS FOR FUNDAMENTAL INVESTIGATION

A Thesis
Presented to
The Academic Faculty

by

David Spencer Mebane

In Partial Fulfillment
of the Requirements for the Degree
Doctor of Philosophy in the
School of Materials Science and Engineering

Georgia Institute of Technology
December 2007

DISCRETE NUMERICAL SIMULATIONS OF SOLID OXIDE FUEL CELL ELECTRODES DEVELOPING NEW TOOLS FOR FUNDAMENTAL INVESTIGATION

Approved by:

Prof. Meilin Liu, Advisor
School of Materials Science and Engineering
Georgia Institute of Technology

Prof. Yingjie Liu
School of Mathematics
Georgia Institute of Technology

Prof. David McDowell
School of Materials Science and Engineering
Georgia Institute of Technology

Prof. Ian Ferguson
School of Materials Science and Engineering
Georgia Institute of Technology

Prof. Tom Fuller
School of Chemical and Biomolecular Engineering
Georgia Institute of Technology

Date Approved: 13 November 2007

This work, and the career that it may launch, are dedicated to the earth and its inhabitants, whom God made good.

ACKNOWLEDGEMENTS

There are many to thank. First are those without whom the technical work here would not be possible. I am very grateful for the guidance, support and trust of Professor Meilin Liu. Professor Yingjie Liu has also been indispensible from a technical standpoint. Many in Prof. Meilin Liu's workgroup have contributed to the furthering of this course of study, some significantly: Yongman Choi, Songho Choi, Chuck Compson, Erik Koep, Xiaoyuan Lou, Matt Lynch, Jeng-Han Wang, Robert Williams and Lei Yang all deserve mention.

Then there are those without whom I would not be here to help establish this course of study. My professors in Mechanical Engineering at Rice University, Alan Chapman, Chao-Cheng Wang and Yildiz Bayazitoglu, demonstrated with their letters of support that they had more faith in me than I had in myself when I attended Rice. Professor Tom Sanders and Mrs. Susan Bowman showed enough open-mindedness to invite an application from a highly motivated individual with a suspect academic track record. Scott Greene and Jennifer Mullins at Georgia Tech Financial Aid made sure that my attendance would be fiscally possible. Professor Rosario Gerhardt, with assistance from Professor Arun Gokhale, guided me through my Master's study, which led the way toward my work in the science of energy. Thanks go again to Prof. Liu for having faith enough in me to choose me for his workgroup and entrust me with establishment of this course of study.

Most importantly, I must thank my family. First is my lovely wife Rebecca, who never complained about the financial hardship my study placed on us, but always encouraged me to pursue what matters most. My wonderful little girl, Scarlet, who so far has taught me more than I've been able to teach her, and my baby boy, Spencer, who I'm sure will do the same. My parents, John and Carol, have relieved my financial burden, but more importantly, never gave up hope for me, even when given ample reason to do so. I am lucky to count my brother and sister, Alan and Hannah, as two of my best friends.

TABLE OF CONTENTS

LIST OF TABLES

LIST OF FIGURES

SUMMARY

The cathode is one of the most important components for development in solid oxide fuel cells (SOFCs). The reduction of oxygen at the cathode is the slow step in the cell reaction at low temperatures, meaning that improvements in cathode performance translates directly to higher cell power densities and lower costs per kilowatt.

Understanding of the reaction process at the cathode is key to its development, but quantitative understanding of cathodic oxygen reduction has been hard to come by due to the complexity of the reaction. In mixed ionic-electronic conductors (MIECs), such as the dominant $La_xSr_{1-x}MnO_{3\pm\delta}$ (LSM), the reduction process includes adsorption and dissociation of the gas, both surface and bulk transport pathways, oxygen transfer at the LSM-electrolyte interface and a triple-phase boundary (TPB) reaction. The existence of each of these aspects of the reaction is fairly well established; quantitative characterization remains lacking.

A program of study for solid oxide fuel cell (SOFC) cathodes has been established. The program involves the design and fabrication of test cells which simplify the reaction process (blocked electrodes and dense thin films) or restrict each step to a well-known geometry (patterned electrodes), while reducing the dimensionality of the corresponding model to two dimensions or less. The results of electrochemical testing are then compared rigorously and quantitatively to the model using a non-gradient optimization technique and robust test for uniqueness.

Specific results have been achieved in the areas of surface modeling for air-MIEC reactions, sheet resistance in mixed conductors, defect equilibrium in LSM and a new model for the interface between LSM and the electrolyte yttria-stabilized zirconia.

CHAPTER I

INTRODUCTION

Solid oxide fuel cells (SOFCs) may not ultimately solve the world's crisis of energy, but they are achievable in the short-term, integrable with current energy streams and much more efficient than the current energy conversion infrastructure. The existence of many operating installations worldwide is testament to their achievability. The most prominent reason behind this roll-out is that SOFCs run on natural gas – which is readily available in most urban areas – as well as hydrogen. The high electrical conversion efficiency (50% as a practical matter) combined with very good scalability, such that stacks can be designed for micro-power applications all the way up to power plants, means that fossil fuels can be utilized very efficiently. For combined heat and power applications the thermal efficiency may increase even higher; if every home and business were equipped with SOFC stacks operating on natural gas or gasified coal, greenhouse emissions in this country would be a fraction of what they are today, and much of the power carrying infrastructure could be dismantled. The stage would also be set for use of renewable fuels, since SOFCs run just as well on hydrogen as methane. The off-gas from SOFCs can also be used in gas turbines to boost electrical conversion efficiencies at a power plant 10% or more.

Of course, despite its promise, there are still several problems in the electrochemical operation of SOFCs which keep the technology still firmly within the niche market category. Many of these difficulties are related to poisoning of cell components during normal operation – in particular, the standard anode of nickel and yttria-stabilized zirconia (YSZ) is sensitive to sulfur poisoning, and at lower temperatures (or in heavier carbon-based fuel streams), coking. The standard cathode, strontium-doped lanthanum manganate (LSM) is sensitive to chromium poisoning from the stainless steel cell interconnects. The high temperature of the cell itself, which is an advantage for fuel reforming purposes, is a hinderance in a thermo-mechanical context, since the seals between fuel and air compartments must

be ceramic, and are therefore both expensive and prone to failure during thermal cycling.

Whatever the problems of SOFCs, better understanding of the cell's operation shows the way to the solutions. As a concrete example, it can be expected that new and better cathode microstructural designs will follow when the resistances of various steps in the reduction of oxygen have been quantified.

The primary contribution of this work is the design and initial implementation of a long-term program that will lead to better understanding of the electrochemistry of SOFC operation. The program involves simple, routine electrochemical experiments performed on novel, precisely designed and fabricated test cells, that are compared with sophisticated electrochemical models in a rigorous way in order to quantify the behavior of cell components. It is expected that the tools developed in the course of this work will be useful for the study of many different materials and cell components.

The component chosen for the initial study, on which this work focuses its practical undertakings, was the cathode. The specific material was LSM, in particular $La_{0.8}Sr_{0.2}MnO_{3\pm\delta}$, which is currently the dominant cathode material in the industry.

1.1 The state of knowledge for oxygen reduction on LSM

A brief survey of electrochemical studies on LSM will underscore the challenges inherent in studying this material, and motivate the actions taken in pursuit of a better, quantitative understanding.

1.1.1 General

There are now several reviews on the topic of oxygen reduction on LSM available,[1, 17, 32, 59, 72, 83, 95, 96] and much knowledge has been gained over the past two decades. However, as the cited reviews will attest, there are considerable gaps. Notably, there are still unanswered questions on the defect structures for LSM and that of the interfaces with the gas and typical electrolyte materials such as YSZ. Our quantitative knowledge of bulk and surface transport properties is also deficient, and there is little knowledge of the reaction sequence at the gas-exposed surface.

The overall reaction for a p-type, oxygen-conducting SOFC cathode (such as LSM) is:

$$\frac{1}{2}\mathrm{O_2(gas)} + \mathrm{V_O^{\cdot\cdot}} \rightarrow \mathrm{O_O^x} + 2\mathrm{h^{\cdot}} \tag{1}$$

where, in the Kröger-Vink notation, $\mathrm{V_O^{\cdot\cdot}}$ denotes an oxygen vacancy in the solid state with two effective positive charges (with respect to the perfect crystal), $\mathrm{O_O^x}$ denotes a neutral oxygen ion in a solid state oxygen site, and $\mathrm{h^{\cdot}}$ denotes a positively charged electron hole. However, the reaction divides into several elementary steps, including:

- adsorption of gaseous molecular oxygen
- reduction and dissociation of the adsorbed molecule in multiple steps
- diffusion of adsorbates to various incorporation sites on the MIEC surface and at the triple phase boundary (TPB) between air, the MIEC and the electrolyte
- transport of vacancies to the incorporation sites
- transport of electron holes away from the reduction sites
- the incorporation reaction (combination of adsorbed atomic oxygen and oxygen vacancies)

and

- the transfer of vacancies from the electrolyte into the MIEC.

Early electrochemical experiments focused on drawing distinctions between bulk-mediated and surface-mediated processes in the cathodic reaction (1). The bulk-mediated process involves diffusion of oxygen through a bulk phase, while the surface-mediated process involves diffusion of oxygen across a surface. Thin film experiments on LSM showed a linear thickness dependence for the electrode resistance, suggesting a bulk-mediated process.[26, 27, 45, 53, 54, 77] However, experiments on porous electrodes or cracked films suggested that resistances in LSM frequently scale with the TPB length, with lower resistances than their dense-film counterparts.[77, 28, 93] This points to a surface-mediated mechanism.

The data from patterned electrodes[60, 11, 7] also shows that both bulk and surface contributions can be active, depending on the geometry. These parallel paths of surface and bulk greatly complicate our ability to get a quantitative grip on the reaction mechanism. Moreover, LSM displays a decreased electrode resistance at high cathodic potentials or after extended cathodic polarization.[77, 69, 94] These phenomena may reflect an increase in the oxygen deficiency near the electrolyte interface under applied cathodic potential,[42, 50] and changes in cathode surface structure,[65, 48, 49, 107] respectively.

By contrast, given the high electronic transference numbers of both materials, and data provided through electronic measurements such as the four-point probe and thermoelectricity, there is greater confidence in electronic structure and transport models. These generally depict a hopping mechanism involving e_g and t_{2g} energy levels of the Mn ion in LSM.[88, 79, 51]

Techniques for measuring surface exchange and ionic diffusivity in LSM and related materials include electron blocking, current interrupt and isotope exchange/secondary ion mass spectroscopy (SIMS).[53, 42, 10, 20, 21, 22, 43, 59, 66, 67, 114, 113] But because the overall rate law for the surface reaction is likely nonlinear, and the rate laws for elementary steps depend exponentially on the surface potential, the utility of average measurements (generally taken at or near equilibrium) is limited to small perturbations from equilibrium.

New TEM and electron energy loss spectroscopy (EELS) data on the YSZ-LSM interface shows that La and Mn species inhabit cation sites in YSZ near the interface, leaving behind cation vacancies.[5] This is important information that could lead to a better understanding of the structure of this interface and its role in oxygen reduction, and will be discussed in depth later.

1.1.2 Existing quantitative continuum modeling

1.1.2.1 One-dimensional models and porous electrode theory

Treatments of a one-dimensional, homogeneous medium with multiple charged species using the Nernst-Planck and Poisson equations date back decades. Brumleve and Buck numerically solved the full nonlinear problem in one dimension in 1978.[13] Recently, it became

more popular to follow Brumleve's alternate approach of treating the linearized problem (which is appropriate for low-signal experiments such as impedance spectroscopy) using an "exact" equivalent circuit.[14] Many of the resulting transmission-line circuits apply to MIECs.[8, 47] These approaches are appropriate for thin films with an absence of multi-dimensional effects at the continuum scale.

The most popular modeling technique for MIECs appearing in the literature is a variation on porous electrode theory,[19, 2, 25, 97, 98, 109] as initially developed for porous electrodes submerged in liquid electrolytes. In the context of SOFC electrodes, this approach reduces a porous material to a monolithic continuum, with the reactions at the internal surfaces treated as homogeneous reactions within the system. Combined with an assumption of infinite electronic mobility (not a bad assumption for macroscopic materials) symmetry considerations permit a reduction of the problem domain to one dimension. If a low-overpotential signal is used, the field variables in the resulting equations may be expanded about an equilibrium value and truncated after first-order terms, enabling an analytical solution. Nonlinear results are obtainable through finite difference discretization and Newton's method.[81]

Several porous electrode models considered both bulk and surface transport in LSM, leaving equations in nonlinear form and solving through finite difference discretizations.[19, 25, 97, 98] One such model produced an interesting result in accordance with experimental evidence, showing that, in a relatively poor ionic conductor such as LSM, the reduction process may gradually shift from surface-mediated toward a more active bulk with increasingly negative applied potential.[19]

The principal difficulty with porous electrode theory is its limitation in terms of model geometry; it is linked to a porous structure, probably single-phase due to difficulties incorporating the effects of connectivity. Also, one-dimensional modeling regimes will not suffice for any geometry engendering multi-dimensional effects, as is the case with many patterned electrodes and thin films appropriate for fundamental investigation in LSM.

1.1.2.2 Multi-dimensional simulations

A few multi-dimensional simulations of SOFC cathodes which appeared over the past few years[31, 36, 41, 35] illustrated the benefits of expanding dimensionality. They have addressed issues such as current constriction at TPBs and grain boundaries. However, they have continued to use diffusion-only models, ignoring the possibility of sheet resistance in MIECs.

1.1.3 Bulk defects in LSM

The defect chemistry of LSM has been assessed using for nonstoichiometry experiments.[64, 76, 82, 112] The best of the resulting bulk defect models for LSM[101, 64, 76, 82, 88] depict six major defects, including A and B site cation vacancies, two defective valence states for Mn (one effective positive and the other negative), oxygen vacancies and dopants. The mixture is random. This random model, which was improved upon in the course of this work, predicts high-temperature nonstoichiometry curves well, but fails at low temperatures and also in the prediction of conductivity.

1.2 Framework for quantitative study

The complexity of the LSM-YSZ system demands precisely controlled experiments, as well as unique and detailed models corresponding to those experiments, and robust methods of comparing the two. The established program of study therefore contains three primary development tracks:

- Design and fabrication of test cells that limit the complexity of the reaction or proscribe various processes to areas with well-characterized geometries
- The conversion of basic hypotheses into quantitative physical models appropriate to the test cells, and their corresponding computational implementation
- Development and implemetation of robust methods of optimization

The following chapters chronicle progress made in all three areas to this point in an ongoing project. The first chapter develops a hypothesis on the sequence of oxygen catalysis on the oxygen-exposed MIEC surface into a quantitative physical model applicable to a computational approach. The second chapter uses the results from the first, incorporating them into a quantitative model suitable for thin-film and patterned test cells, and surveys progress made toward the fabrication of these cells. The third chapter focuses on the development of the bulk defect theory for LSM, using the particle swarm optimizer (PSO) to judge the suitability of a new proposal against nonstoichiometry experiments, while simultaneously estimating model parameters. The fourth chapter establishes a new hypothesis for the causes behind the structure seen at the LSM-YSZ interface, and chronicles progress made to date in development of an appropriate physical model and design of test cells for the investigation.

CHAPTER II

CLASSICAL, PHENOMENOLOGICAL ANALYSIS OF THE KINETICS OF REACTIONS AT THE GAS-EXPOSED SURFACE OF MIXED IONIC ELECTRONIC CONDUCTORS

2.1 Introduction

One of the most interesting and dynamic areas of study in the field of MIECs involves the phenomenological picture of reactions occurring on the gas-exposed surface of a charged MIEC. It is not an electrochemical reaction in a traditional, familiar sense: no net current flows across the electrified interface at a nonequilibrium steady state. Yet some elementary steps at the gas surface do involve the transfer of electrons between the bulk MIEC and some adsorbed surface state (see Figure 1). The question then becomes, are the rates of these reactions directly or indirectly controlled by the outside potential applied to the MIEC? The literature reflects some disagreement.[2, 3, 19, 97, 70, 102]

The work of Vayenas and co-workers on the response of Pt surface species to applied potential forces a refinement of the question. Vayenas's work focused on the electrochemical promotion of Pt-catalyzed oxidation reactions. A wealth of experimental data produced in the course of studying this phenomenon indicates that the application of outside potential to a Pt working electrode on a solid electrolyte influences the surface potential through adsorbates on the Pt surface. This, in turn, influences the rate of chemical reactions occurring on the surface. (See [106] and citations therein.) But as Fleig and Jamnik point out in a theoretical analysis inspired by Vayenas's results, the influence of applied potential on the surface potential is not necessarily a direct proportionality, as Vayenas held.[34]

In a subsequent paper, Fleig analyzed the gas surface kinetics problem for MIECs.[33] Fleig's analysis was notable for its use of electrochemical rate expressions to describe surface processes. But the Butler-Volmer style expressions for adsorption and incorporation Fleig started with respond in a direct manner to polarization changes at the MIEC-air interface,

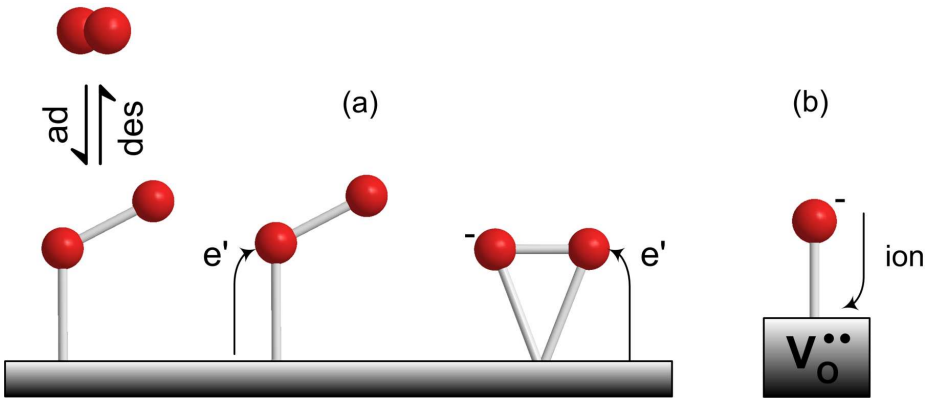

Figure 1: (a) electron transfer from MIEC to the LUMO of oxygen to form O_2' and O_2'' (b) oxygen ions combine with vacancies on the surface of the MIEC. While each step represents a reaction involving charge transfer, the overall reaction results in zero net charge transferred out of the MIEC. Figure created by Yongman Choi.

as opposed to the overpotential applied to the MIEC. Again, the results show a complex relationship between the overpotential applied at the electrode and the change in surface potential, which is the driving force for the reactions. This work is a significant step forward in our theoretical understanding of gas-surface reactions on MIECs.

This work will complement Fleig's in two respects. First, we provide a derivation of the relevant phenomenological rate expressions from first principles. Second, we incorporate these expressions into a phenomenological model of an MIEC cathode and use the results to draw conclusions affecting the debate on whether the reactions occurring at the surface can be described by purely chemical rate expressions.

The following analysis will follow the electrochemical potential-transition state theory derivation first published by Parsons,[84] but also appearing in Erdey-Gruz,[29] Delahay[23] and Bockris, *et al.*[9] The analysis contains several assumptions, although these assumptions do not prevent general conclusions from being drawn on the kinetic phenomenology at MIEC-gas interfaces. The discussion following the analysis presents a pair of examples that, while not universal, nonetheless illustrate some important implications.

2.2 Analysis

Consider the reaction at the oxygen-exposed surface of an MIEC electrode conducting oxygen vacancies and electron holes under cathodic polarization, written above in equation

(1). Now consider a simple breakdown of equation (1), into dissociative adsorption and incorporation steps:

$$\frac{1}{2}\mathsf{O}_2 + s \rightarrow \mathsf{O}'_{\mathsf{ads}} + \mathsf{h}^{\cdot} \tag{2}$$

$$\mathsf{O}'_{\mathsf{ads}} + \mathsf{V}^{\cdot\cdot}_{\mathsf{O}} \rightarrow \mathsf{O}^{\mathsf{x}}_{\mathsf{O}} + \mathsf{h}^{\cdot} \tag{3}$$

where s represents an adsorption site on the surface of the MIEC. Figure 2 depicts the standard free energy surface along a reaction coordinate for a reaction under cathodic polarization. Applying the figure to reaction (2), the standard free energies for states I and II are:

$$\bar{\mu}^0_{I,2} = \frac{1}{2}\mu^0_{\mathsf{O}_2} \tag{4}$$

$$\bar{\mu}^0_{II,2} = \mu^0_{\mathsf{O}'} - F\phi_s + \mu^0_{\mathsf{h}} + F\phi_m \tag{5}$$

where ϕ is the electrostatic potential and the subscripts m and s refer to the MIEC just beneath the surface and on the MIEC surface, respectively. The key to the derivation is the introduction of the transfer coefficient, α, which allows for the definition of the electrical part of the free energy in the activated state:

$$\bar{\mu}^0_{A,e} - \bar{\mu}^0_{I,e} = \alpha\left(\bar{\mu}^0_{II,e} - \bar{\mu}^0_{I,e}\right) \tag{6}$$

where the subscript e refers to the electrical part of the electrochemical potential. Equation (6) leads to an expression for the standard free energy of the activated state:

$$\bar{\mu}^0_{A,2} = \mu^0_{A,2} + \alpha_2 F\left(\phi_m - \phi_s\right) \tag{7}$$

According to transition state theory (TST), the rate constant of any elementary chemical reaction is given by:

$$k = \kappa\frac{k_B T}{h_P}\exp\frac{-\Delta G^0_A}{RT} \tag{8}$$

where κ is the transmission coefficient, k_B is Boltzmann's constant, h_P is Planck's constant and ΔG^0_A is the standard activation energy. Equations (4), (5), (7) and (8) now yield

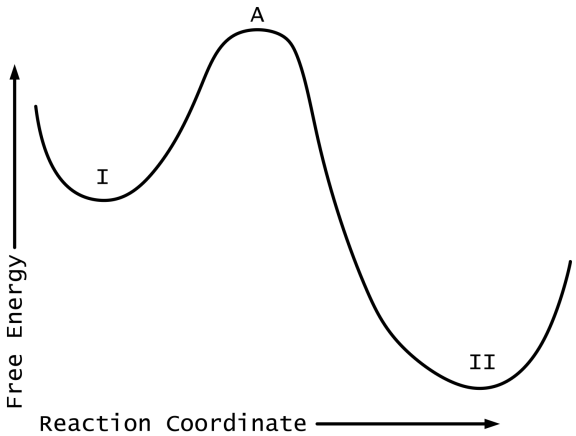

Figure 2: Reduced dimensionality free energy surface for charge transfer reactions.

expressions for the forward and backward rate constants in reaction (2):

$$\overrightarrow{k}_2 = \overrightarrow{\kappa}_2 \frac{k_B T}{h_P} \exp \frac{-\left(\mu^0_{A,2} - \mu^0_{\mathsf{O}_2} + \alpha_2 F\chi\right)}{RT} \tag{9}$$

$$\overleftarrow{k}_2 = \overleftarrow{\kappa}_2 \frac{k_B T}{h_P} \exp \frac{-\left(\mu^0_{A,2} - \mu^0_{\mathsf{O}'} + (\alpha_2 - 1) F\chi\right)}{RT} \tag{10}$$

where $\chi = \phi_m - \phi_s$ is the surface potential. The forward and backward rates for the reaction are therefore:

$$\overrightarrow{r} = \overrightarrow{k}'_2 \exp \frac{-\alpha_2 F\chi}{RT} a^{1/2}_{\mathsf{O}_2} a_{\mathsf{s}} \tag{11}$$

$$\overleftarrow{r} = \overleftarrow{k}'_2 \exp \frac{(1-\alpha_2) F\chi}{RT} a_{\mathsf{h}} a_{\mathsf{O}'} \tag{12}$$

where the k' terms are a set of collected constants and a represents the activity. Assuming dilute concentrations of surface species and holes, and ideal gas, the following expression emerges for the overall rate of reaction 2:

$$r_2 = \overrightarrow{k}''_2 \exp\left[\frac{-\alpha_2 F\chi}{RT}\right] P^{1/2}_{\mathsf{O}_2} \Gamma(1-\theta) - \overleftarrow{k}''_2 \exp\left[\frac{(1-\alpha_2) F\chi}{RT}\right] c_{\mathsf{h}} \Gamma\theta \tag{13}$$

where θ is the occupied site fraction, Γ is the total density of surface sites, and c_{h} is the concentration of holes at the MIEC surface. The k'' terms now include activity coefficients, assumed constant.

When reaction 2 is at equilibrium, $r = 0$. The forward and backward terms are then both equal to a constant, which is the exchange rate:

$$k^0_2 = \overrightarrow{k}''_2 \exp\left[\frac{-\alpha_2 F\chi_0}{RT}\right] P^{1/2}_{\mathsf{O}_2,0} \Gamma(1-\theta_0) = \overleftarrow{k}''_2 \exp\left[\frac{(1-\alpha_2) F\chi_0}{RT}\right] c_{\mathsf{h},0} \Gamma\theta_0 \tag{14}$$

Factoring out k^0 from (13) yields the familiar form of the equation:

$$r_2 = k_2^0 \left[\frac{P_{\mathsf{O}_2}^{1/2}(1-\theta)}{P_{\mathsf{O}_2,0}^{1/2}(1-\theta_0)} \exp \frac{-\alpha_2 F \Delta\chi}{RT} - \frac{c_{\mathsf{h}}\theta}{c_{\mathsf{h},0}\theta_0} \exp \frac{(1-\alpha_2)F\Delta\chi}{RT} \right] \tag{15}$$

where $\Delta\chi = \chi - \chi_0$.

Turning attention to reaction (3), the relevant standard electrochemical potentials are:

$$\bar{\mu}_{I,3}^0 = \mu_{\mathsf{O}'}^0 - F\phi_s + \mu_{\mathsf{v}} + 2F\phi_m \tag{16}$$

$$\bar{\mu}_{II,3}^0 = \mu_{\mathsf{h}}^0 + F\phi_m \tag{17}$$

$$\bar{\mu}_{A,3}^0 = \mu_{A,3}^0 + F\left(2\phi_m - \phi_s\right) + \alpha_3 F\left(\phi_s - \phi_m\right) \tag{18}$$

Taking the analysis through the same procedure as above, the forward and backward rate constants are therefore:

$$\overrightarrow{k}_3 = \overrightarrow{\kappa}_3 \frac{k_B T}{h_P} \exp \frac{-\left(\mu_{A,3}^0 - \mu_{\mathsf{O}'}^0 - \mu_{\mathsf{v}} - \alpha_3 F\chi\right)}{RT} \tag{19}$$

$$\overleftarrow{k}_3 = \overleftarrow{\kappa}_3 \frac{k_B T}{h_P} \exp \frac{-\left(\mu_{A,3}^0 - \mu_{\mathsf{h}}^0 - (\alpha_3 - 1)F\chi\right)}{RT} \tag{20}$$

This leads to the expression for the rate of reaction (3):

$$r_3 = \overrightarrow{k}_3'' \exp\left[\frac{\alpha_3 F\chi}{RT}\right] c_{\mathsf{v}}\Gamma\theta - \overleftarrow{k}_3'' \exp\left[\frac{-(1-\alpha_3)F\chi}{RT}\right] c_{\mathsf{h}}\Gamma(1-\theta) \tag{21}$$

and the corresponding introduction of an exchange rate constant:

$$r_3 = k_3^0 \left[\frac{c_{\mathsf{v}}\theta}{c_{\mathsf{v},0}\theta_0} \exp \frac{\alpha_3 F\Delta\chi}{RT} - \frac{c_{\mathsf{h}}(1-\theta)}{c_{\mathsf{h},0}(1-\theta_0)} \exp \frac{-(1-\alpha_3)F\Delta\chi}{RT} \right] \tag{22}$$

2.3 Implications

Since α is always a positive constant between 0 and 1 (assuming the reaction is an elementary step) the results presented in equations (15) and (22) illustrate that if both adsorption and incorporation reactions are thermally activated, the effect of the surface potential on the rates of these steps must be opposing. (That is, tending to increase the rate of one and to decrease the rate of the other.) The observation that $r_2 = r_3$ at steady state leads to a significant implication: the chemical (pre-exponential) terms in equations (15) and (22)

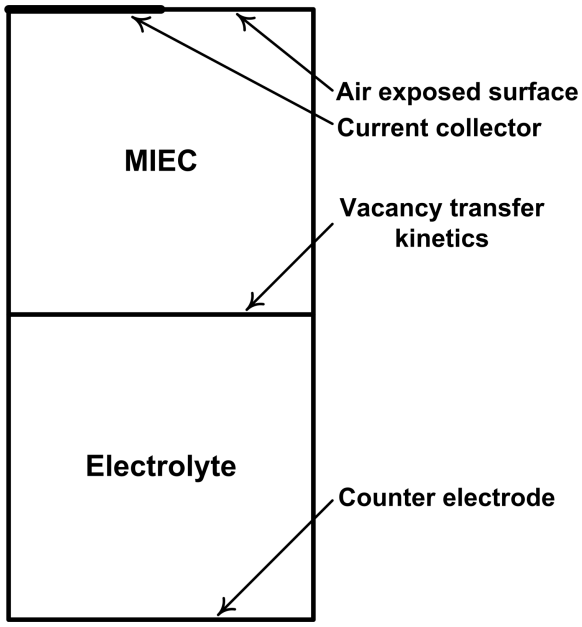

Figure 3: Schematic of the model geometry for the MIEC half cell model. The vertical sides on each side are considered to be symmetrical boundaries.

must play a dominant role in one or both reactions, leading to practical chemical control of the rate of reactions.

To illustrate this point, a 2D model of a dense, patterned MIEC electrode in a half-cell experimental setup was created. The geometry of the test cell appears in Figure 3. The model utilizes the reaction mechanism (2)-(3), and the attending rate expressions (15)-(22) as flux boundary conditions at the air surface of the MIEC. The other features of the model are dilute solution transport theory (with holes and vacancies as mobile defects), no surface diffusion, and electroneutrality. The surface potentials are calculated using a Helmholtz model of the double layer, which allows calculation of the potential difference from the site fraction of adsorbates. The method of solution is an iterative finite volume method. (This model is derived in detail in the next chapter.)

Table 1 lists values for parameters in the model. Most were adapted from approximate data given by Svensson for perovskite MIECs $La_xSr_{1-x}(Co,Mn)O_{3\pm\delta}$ (LSC and LSM).[97, 98] One exception is the equilibrium concentration of holes, which is loosely based on the defect chemistry of LSM, but chosen for the most part in order to create an MIEC rich in electronic species. The other exceptions are the exchange rate constants for adsorption and

Table 1: Parameters used in the simulation

	run 1	**run 2**
$c_{v,0}$	2.0x10^{-4} mol/m^2	same
$c_{h,0}$	300.0 mol/m^2	same
k_2^0	10^{-8} mol/m·s	10^{-2} mol/m·s
k_3^0	10^{-2} mol/m·s	10^{-6} mol/m·s
θ_0	2.0x10^{-3}	same
T	1173 K	same
Γ	10^{-3}	same

incorporation, which hew closely to Svensson's numbers for the first run but were modified for the second as described below. The model geometry is 1 μm square, with a regular mesh size of .01 μm square for run 1 and 0.1 μm square for run 2. (Slower convergence times necessitate a coarser mesh for run 2.) Applied potential across the half cell is -0.1 V for both runs. All transfer coefficients are assumed to be 0.5.

For the first run of the model, the incorporation and adsorption exchange rate constants remain in the ranges given by Svensson, which is to say that the incorporation constant is much lower (by six orders of magnitude). The vacancy distribution in the MIEC is shown in Figure 4. Note that the distribution is nearly uniform, with very gentle concentration gradients leading towards the air surface, but throughout the level is much higher than the equilibrium value for vacancies in the MIEC. The site fraction of adsorbates on the MIEC surface (not shown) is nearly uniform across the surface, and is almost exactly equal to the equilibrium value of the adsorbate concentration. (The numbers are actually higher than equilibrium value listed in Table 1 by much less than 1%.)

This result makes sense in consideration of the mechanism (2)-(3). A high exchange rate constant for the adsorption reaction ensures that (2) stays very close to equilibrium, which means that the concentration of adsorbates and, correspondingly, surface potentials remain close to their equilibrium values. As a result, the potential dependent terms in equation (22) have almost no effect on the rate of incorporation. Instead, the increase in the concentration of vacancies in the MIEC drives the reaction.

The situation changes when the adsorption step becomes rate limiting. For the second

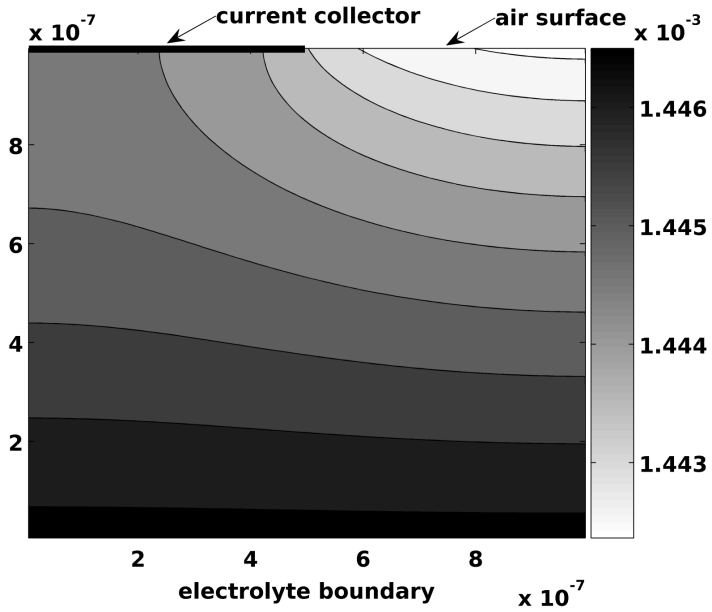

Figure 4: Vacancy distribution in the MIEC, mol/m^2, for model run 1.

run of the simulation, an adsorption rate constant of 10^{-6} mol/m^2-s and an incorporation constant of 10^{-2} mol/m^2-s were used. Figure 5 shows the vacancy distribution, which rises to a similar average value as that of the incorporation limited case, although the gradient in concentration is slightly higher. However, the adsorbate site fraction in this case deviates significantly from equilibrium. The change is negative, with the concentration at steady state approximately 8% less than the equilibrium value on average. This tends to drive the adsorption reaction faster, through both chemical and potential-dependent terms in equation (15). In effect, the surface potential changes in such a manner as to drive the slower adsorption reaction, while the faster incorporation reaction relies on the chemical driving force associated with the change in vacancies.

Which scenario is more likely in an actual cell? Equation (21) shows that the incorporation exchange rate constant, k_3^0, involves a product of the equilibrium concentration of vacancies and the equilibrium site fraction. In MIECs used in solid oxide fuel cells, such as LSM and LSC, both numbers are small. This suggests that incorporation exchange rate constants may be low on the surfaces of these materials. If that is the case, one expects that the concentrations of surface species as a whole on the MIEC surface will not deviate appreciably from equilibrium.

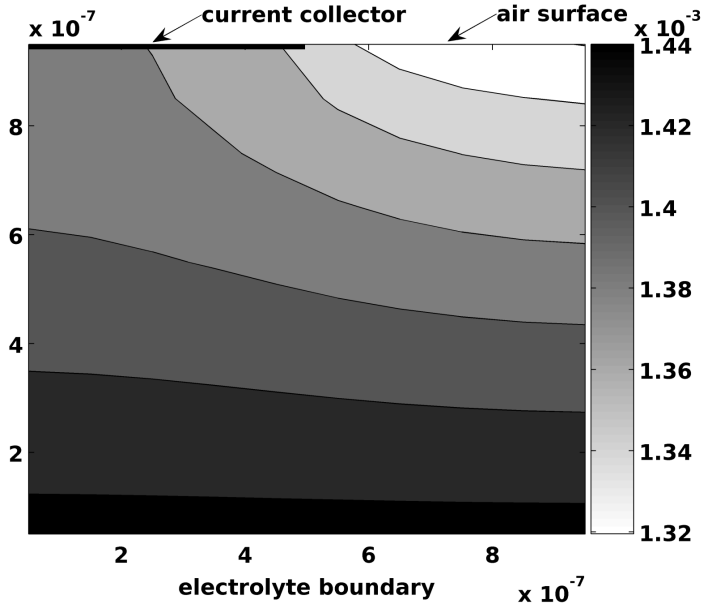

Figure 5: Vacancy distribution in the MIEC, mol/m^2, for model run 2.

This, of course, is the same situation one would expect if the rate expressions were affected by deviations of chemical concentrations from equilibrium only. The effect of the potential-dependent terms is, in general, simply to reinforce the chemical response of the rate of an elementary process to changes in adsorbate concentrations. For an adsorption-dominated mechanism, for instance, the deviation of adsorbate concentration from equilibrium is not as large as it would be in the case of chemical rate control. For more complicated mechanisms involving more than one adsorbed species, the picture becomes more interesting. For example, a buildup of charged, chemisorbed peroxide moeties (O_2'') due to a slow dissociation step would have the effect of increasing the rate of the oxygen incorporation reaction.

CHAPTER III

THIN FILM AND PATTERNED ELECTRODE TEST CELLS AND MODELS: REDUCING COMPLEXITY AND DIMENSIONALITY, AND THE PROBLEM OF SHEET RESISTANCE

Thin films and patterned electrodes are effective vehicles for study of electrodics in MIECs, since it is possible to precisely control the geometry related to triple phase boundary (TPB) and bulk reaction pathways. Many experimental studies involving thin films and patterned electrodes for the electrode MIECs $La_{1-x}Sr_xMnO_{3\pm\delta}$ (LSM) and $La_xSr_{1-x}Co_{1-y}Fe_yO_{3\pm\delta}$ (LSCF) have appeared over the years.[7, 11, 12, 26, 28, 27, 44, 45, 46, 54, 53, 60, 61, 74, 77, 80, 91, 99, 110, 111]

None of these studies has yet combined the kind of experimental control and ingenuity required to create these cells with the theoretical rigor seen in the context of porous electrodes. One reason for this is that these cells – especially those requiring photolithography or other microfabrication processes – are particularly difficult to make. They typically require high-vacuum and sometimes cleanrooms, and many of the materials involved are not standard for the semiconductor industry. Another is that there is no appropriate model framework for the thin-film/patterned electrode geometry. One of the thrusts of the program of quantitative study of which this work forms a part is to solve these problems, by designing useful test cells based on thin and patterned film geometries that limit the compexity of the reactions to be studied, fabricating those cells, and developing physical models appropriate to them.

This chapter will present our results in these areas to this point. These results include the apparently successful fabrication of thin films and patterned electrodes conforming to a design that eliminates the influence of platinum current collectors while enabling the reduction of the problem to two dimensions. We have also successfully derived and implemented two-dimensional computational simulations for the steady-state DC behavior of

these electrodes, which includes a treatment of sheet resistance. Experimental evidence for sheet resistance in thin and patterned MIEC electrodes has been reported, but never before treated theoretically. The behavior of the simulations qualitatively conforms to most of the results on thin and patterned films available in the literature.

3.1 Test cell design and fabrication

As discussed in section 1, one of the difficulties in studying the reduction reaction on LSM is the existence of multiple pathways, each with multiple steps. The advantage of thin film and patterned cell designs is that one gains the power to control the rate of these different steps by controlling the associated geometry. Thin dense films, for instance, eliminate the surface mediated, TPB-dependent pathway. When a TPB is introduced in a patterned film, the ratio of its length to the exposed surface area is easily measured.

We also sought to reduce the dimensionality of our models, by controlling the symmetry of the patterned cells. The idea is shown here in Figure 6. What the figure depicts is simply a thin, dense film of LSM deposited on YSZ, with patterned platinum current collectors deposited on top as long stripes. If the stripes are long enough, and there are enough of them, and if additionally the size and placement of the counter electrode is carefully controlled, we can ignore edge effects and the model can be reduced to the dashed-line box shown in the cross-section of Figure 6b).

A TPB can be introduced by patterning gaps in the LSM film in strips parallel to the current collectors. This retains the two-dimensional aspect of the model. Finally, the adsorption reactions at the platinum surface can be avoided by depositing an inert cover (such as undoped ZrO_2). A cross-section of the final designs are shown in Figure 7.

Patterned cells fitting this design have been successfully fabricated using photolithography and plasma sputtering; optical images appear in Figure 8. The photolithography and sputtering of platinum was performed by Xiaoyuan Lou; sputtering of LSM and undoped zirconia was performed by Songho Choi. LSM targets for sputtering were prepared by Matt Lynch and Lei Yang through solid-state reaction. The next step in the process will be the affixing of a porous platinum or silver counter electrode, followed by electrochemical testing

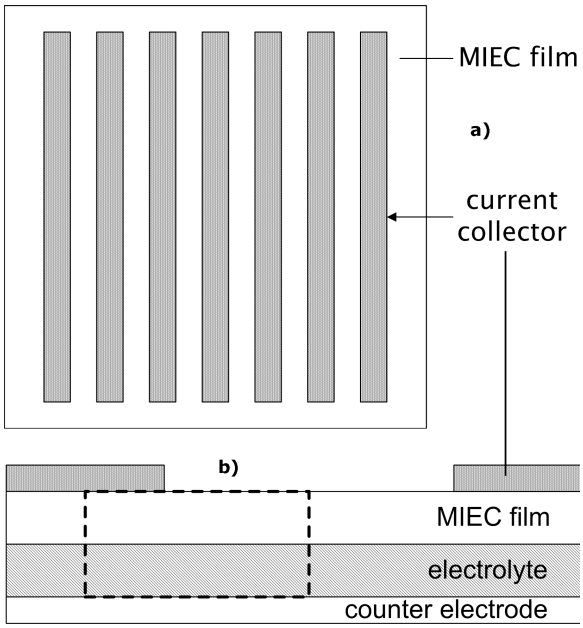

Figure 6: a) Top view and b) cross-sectional view of the cell geometry. The dashed-line box in part b) indicates the smallest symmetrical element in the cross-section, which is used as the model geometry for thin films.

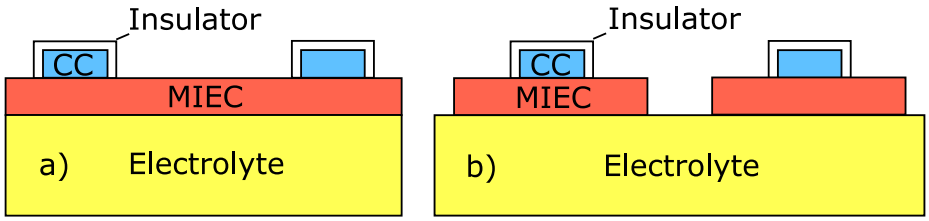

Figure 7: Cross-sectional a) thin film and b) patterned cell with TPB schematics. Figure originally created by Matt Lynch.

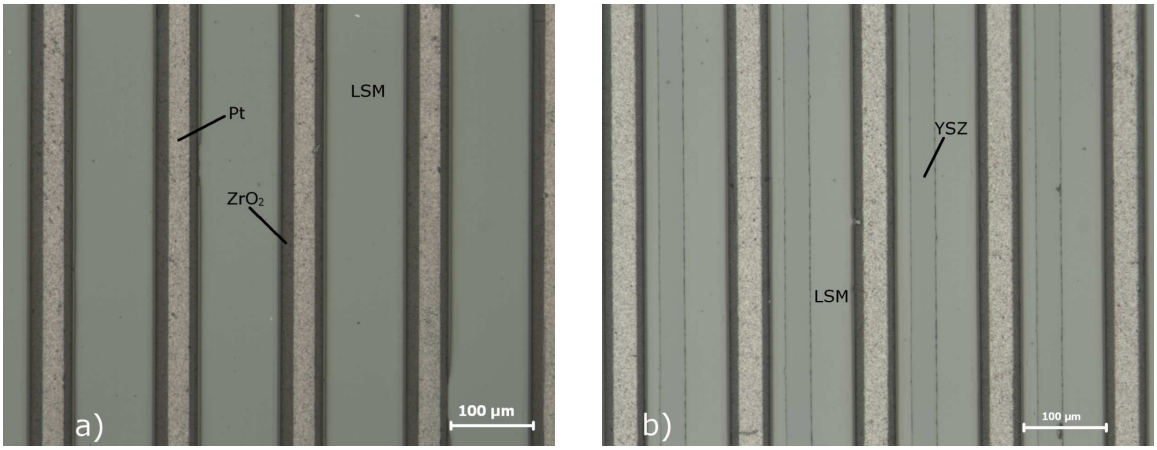

Figure 8: Optical images of patterned electrodes a) without and b) with TPB. Electrodes produced in collaboration with Xiaoyuan Lou, Songho Choi, Matt Lynch and Lei Yang. Images by Matt Lynch.

using potential-dependent impedance spectroscopy (IS).

3.2 Sheet resistance in thin MIEC electrodes

Modeling studies on MIECs to date have avoided consideration of sheet resistance, by assuming either perfect current collection (an implicit assumption in any one-dimensional model)[13, 14, 47] or uniform Fermi level throughout the material.[2, 97, 98, 31, 35, 19, 109, 24] Such assumptions are usually valid for a macroscale electrode, since electronic conductivities far outstrip their ionic counterparts in the most popular MIECs for electrode applications. However, some studies on $La_{0.8}Sr_{0.2}MnO_{3\pm\delta}$ (LSM20) patterned electrodes found evidence of a sheet resistance effect, which calls these assumptions into question for the case of high aspect ratio.[11, 61] These results force a reconsideration of the effects of sheet resistance if patterned electrodes and thin films are to be more widely used for scientific inquiry, and if nanostructured electrodes are to be considered for high performance applications.[108, 89, 71]

A rigorously derived model explicitly treating the effects of both ionic and electronic transport in thin film MIECs has been developed. The simulation treats the case of steady-state DC polarization in the linear or nonlinear response regime on a two-dimensional domain. The application of nonlinear numerical schemes for the treatment of multiple species in one dimension is a relatively well-studied problem.[13, 30] However, the multi-dimensional

case can present difficulties for numerical analysis, especially with mixed boundary conditions.

Using parameter data collected from the literature, the simulation shows that sheet resistance will play an important role for thin LSM films contacted by moderate-sized Pt mesh at moderate to high overpotentials, but not in the limit approaching zero polarization. The shape of the model-generated I-V curves, which conform to most found in the literature for LSM thin films, are dissected in terms of rate-limiting steps, which are bulk ionic transport and sheet resistance for our parameterization. However, when compared to experiment, we find that the electrode resistance generated by the model in the low-polarization limit is considerably higher. Possible reasons for this divergence are discussed.

3.2.1 Model

The model geometry is shown in the dotted-line box of Figure 6. As mentioned in the previous section, the thin-film patterned design allows for a two-dimensional simulation space, with a lack of reactions at the platinum current collector (due to shielding) and at the LSM-YSZ-air TPB.

The overall reaction is shown in equation (1). For the purpose of building the model, we assume the simple reaction sequence (2)-(3), leading to the rate equations (15)-(22). We further assume, however, that there is no pressure drop at the electrode surface, and therefore the partial pressure terms drop out of equation (15).

The flux of species k in the MIEC and electrolyte is:

$$N_k = -u_k c_k \nabla \mu_k \tag{23}$$

where u_k is the mobility, c_k the concentration and μ_k the electrochemical potential of species k. If we adhere to a strictly dilute model, which should usually be valid for mobile species in LSM, we can re-write the above flux in terms of the concentration and the electrostatic potential:[81]

$$N_k = -RTu_k \nabla c_k - z_k F u_k c_k \nabla \phi \tag{24}$$

where z_k is the formal charge on species k, and ϕ is the electrostatic potential. If we assume that only vacancies and holes are mobile, with the (negatively charged) cation

defects essentially immobile, then the values for k are v and h in the MIEC and v only in the electrolyte.

The mass continuity equation is:

$$\frac{\partial c_k}{\partial t} = -\nabla \cdot N_k + G_k \tag{25}$$

where G_k is the net generation rate of species k, which is zero for all species in the bulk phases. The principle of electroneutrality is a very good approximation in the bulk phases, and we employ it even though it prevents a detailed description of the interfaces:

$$F \sum_k z_k c_k + \rho_b = 0 \tag{26}$$

where ρ_b denotes the background charge. Combining equations (23), (25) and (26) in the MIEC produces a coupled system of equations in c_v and ϕ. In the electrolyte, electroneutrality leads to a constant $c_{\mathsf{v},e} = c_{\mathsf{v},e0}$, where the subscript e denotes the electrolyte, and the equation of state becomes Laplace's equation.

The boundary conditions are the potential applied across the current collector and the counter electrode, which are considered to be reversible interfaces, with a grounded counter and no loss in the external circuit. A zero-flux condition holds at symmetrical boundaries, and the rate expressions (15) and (22) define the flux of vacancies at the air-exposed surface. In addition to the air-surface reactions, The vacancy transfer from the electrolyte to the MIEC is an electrochemical reaction, whose rate law (derived according to the method discussed in chapter 2), obeys the following equation:

$$r_\mathsf{i} = k_\mathsf{i}^0 \left[\exp \frac{2\alpha_\mathsf{i} F \Delta\chi_\mathsf{i}}{RT} - \frac{c_\mathsf{v}}{c_{\mathsf{v},0}} \exp \frac{-2\left(1-\alpha_\mathsf{i}\right) F \Delta\chi_\mathsf{i}}{RT} \right] \tag{27}$$

where the value of c_v is taken at the interface. Assuming zero interfacial polarization at equilibrium, the $\Delta\chi_\mathsf{i}$ term in equation (27) is the jump in electrostatic potential across the electrolyte/MIEC interface.

3.2.2 Discretization

We derived a conservative, finite volume discretization that is second-order in space and first-order in time. Keeping time dependence in the solver (the solution effectively iterates to steady-state) enables its linearization through mixing of implicit and explicit terms.

Defining the MIEC domain by a set of rectangular control volumes $\{P_{i,j}\}$, we integrate equation 25 over the cell area located at (x_i, y_j). This yields the standard form for a semi-discrete finite volume scheme:

$$\frac{\partial \hat{c}_{i,j}}{\partial t} = -\frac{1}{\Delta x}\left(\hat{N}_{i+1/2} - \hat{N}_{i-1/2}\right) - \frac{1}{\Delta y}\left(\hat{N}_{j+1/2} - \hat{N}_{j-1/2}\right) \tag{28}$$

where the carat indicates averages over the cell area (for $\hat{c}$) and cell boundary ($\hat{N}$). We then apply the backward Euler time discretization:

$$\hat{c}_{i,j}^{n+1} - \hat{c}_{i,j}^{n} = -\frac{\Delta t}{\Delta x}\left(\hat{N}_{i+1/2}^{n+1} - \hat{N}_{i-1/2}^{n+1}\right) - \frac{\Delta t}{\Delta y}\left(\hat{N}_{j+1/2}^{n+1} - \hat{N}_{j-1/2}^{n+1}\right) + \mathcal{O}\left(\Delta t\right) \tag{29}$$

where the superscript n refers to the value at time t_n. We approximate N at a cell boundary based on the field values in neighboring cells:

$$\hat{N}_{i+1/2}^{n+1} = -\frac{RTu}{\Delta x}\left(\hat{c}_{i+1,j}^{n+1} - \hat{c}_{i,j}^{n+1}\right) - \frac{zFu\left(\hat{c}_{i,j}^{n} + \hat{c}_{i+1,j}^{n}\right)}{2\Delta x}\left(\hat{\phi}_{i+1,j}^{n+1} - \hat{\phi}_{i,j}^{n+1}\right) + \mathcal{O}\left(\Delta x^2\right) \tag{30}$$

The restriction of the concentrations in the drift term to the n^{th} time level allows for a linear solver, which greatly increases the available options. Since the MIEC equations cannot be decoupled, we solved them successively, using the equation written for vacancy conservation to solve for vacancy flux while keeping electrostatic potential constant, then using the hole conservation equation to solve for electrostatic potential while keeping vacancy concentration constant, repeating the process until steady-state is reached. We used a line-by-line iterative solver for each step.[85]

For the parameters listed in Table 2, a geometry of 400 μm in the breadth of current collector and 400 μm between current collectors, film heights from 50-1000 nm, and at moderate cathodic overpotentials (down to -750 mV), the scheme stabilized with respect to the mesh at a cell count of 60 in the MIEC y-direction (the thin dimension of the film) and 100 in the x-direction. The scheme stabilized with respect to the time step at $\Delta t = 10^{-5}$. The iterations to each time step terminated when the change in the infinity-norm of the vacancy vector (equal to its largest element) from that of the previous iteration was less than 0.1%. The simulation stopped when the current of vacancies at the electrolyte interface, matched that of vacancies and holes at the air surface to within 0.01%. Convergence was

Table 2: Parameters gathered from the literature for LSM20

Parameter	Value	Units
$c_{\mathsf{v},0}$	3.0 x 10^{-5}	mol/m^3
$c_{\mathsf{h},0}$	1.1 x 10^{4}	mol/m^3
k^0_{inc}	6.7 x 10^{-7}	mol/m^2·s
u_{v}	2.6 x 10^{-14}	mol·m^2/J·s
u_{h}	1.4 x 10 $^{-12}$	mol·m^2/J·s
$c_{\mathsf{v},e0}$	5.0 x 10^{2}	mol/m^3
$u_{\mathsf{v},e}$	5.8 x 10^{-14}	mol·m^2/J·s

fast – usually a matter of a few seconds, although this could extend to several minutes depending on overpotential, film thickness and the specific parameters.

3.2.3 Parameters

We require reliable data for a number of physical parameters. We sought data for LSM20 and 8% Y_2O_3-doped ZrO_2 at an operating temperature of 750 °C in air. We obtained estimates for all required parameters except k^0_{v}.

The equilibrium concentration of oxygen vacancies in LSM20 at atmospheric P_{O_2} cannot be directly measured, and must therefore be calculated using classical defect models derived from nonstoichiometry data[64, 101, 82, 76, 88] or thermodynamic models derived from phase equilibria.[38] Because it is broad in its consideration of defect phenomena yet straightforward in presentation, we used the classical defect model developed by Poulsen.[88] Poulsen's model requires three equilibrium constants, estimated from nonstoichiometry data. We obtained these constants from Nowotny and Rekas ("random defect model").[82] We should mention that Nowotny and Rekas's method of calculating equilibrium constants from nonstoichiometry data seems somewhat inexact, as gravimetry-derived deviations from stoichiometry are used interchangably with vacancy concentration in their calculations, apparently without regard to the influence of cation vacancies. However, Nowotny and Rekas's listing of standard enthalpies and entropies is convenient for conversion of the data to different temperatures, and the constants thus calculated are easily converted to the form required by Poulsen's model. Calculating the values of equilibrium constants at 750 °C for the Schottky reaction, reduction of LSM and disproportionation of Mn from Nowotny and

Rekas's data, and employing Poulsen's technique for the small polaron model in Matlab® code (with A-site nonstoichiometry assumed to be 5%), yielded the values for $c_{\mathrm{v},0}$ and $c_{\mathrm{h},0}$ reported in Table 2.

Kilner noted a correlation between the diffusivity of oxygen tracer atoms and the effective surface exchange constants in MIECs used for SOFC cathodes.[59] This correspondence suggests that the reactions at the air-exposed surface in these MIECs are rate limited by some step involving oxygen vacancies at the surface (although the exact nature of this step is not yet known). In our surface model (2)-(3), the only reaction involving oxygen vacancies is the incorporation step (3). We therefore assume that the incorporation step is rate-limiting, and reaction (2) is in equilibrium.

This assumption carries several implications. First, it is no longer important to find an accurate value for k^0_{ads}, it must simply be considerably higher than k^0_{inc}. Second, an equilibrated adsorption step – combined with the fact that in the case of LSM the concentration of holes is always much larger than that of vacancies – means that the concentration of adsorbates on the surface will not deviate appreciably from equilibrium. Since the deviation of the adsorbate concentration from equilibrium controls the surface potential, $\Delta\chi \approx 0$. Third, the value for the equilibrium site fraction, θ_0, is not important.

The final implication of incorporation rate control at the surface is that the average exchange constant measured via isotope exchange / SIMS and the exchange rate constant k^0_{inc} of our model are the same. With that in mind, we used DeSouza and Kilner's measurement of the oxygen exchange rate constant.[21] We also used DeSouza's isotope exchange / SIMS measurement of the oxygen tracer diffusivity and activation energy in LSM20, which along with the formula $D^* = f^* D_v \left[\mathsf{V}^{\cdot\cdot}_{\mathsf{O}}\right]$, where D^* is the tracer diffusion coefficient and f^* is the tracer correlation factor (equal to 0.69), yields the diffusivity of vacancies.[20] The mobility then follows directly from the Nernst-Einstein relation. These values are reported in Table 2.

Because of its high electronic transference number, the electronic conductivity of LSM20 can be accurately measured. The electronic conductivity at 750 °C was calculated from conductivity and activation energy data reported in Minh and Takahashi,[75] and the mobility

of electron holes follows from the conductivity. Oxygen vacancy concentration in the electrolyte was calculated by assuming a full ionization of acceptor dopants ($\mathsf{Y}'_{\mathsf{Zr}}$) and 100% compensation by oxygen vacancies. Ionic conductivity data[75] was then converted into the value for $u_{\mathsf{v},e}$ appearing in Table 2.

We assume that the transfer coefficient in equation (27) is 1/2.

As mentioned, the only parameter whose estimate eluded us is that of the exchange rate constant at the LSM-YSZ interface, k^0_{v}. Our literature search revealed no attempts at direct measurement of this parameter, but a parametric study by Baumann, *et al.* indicated that the vacancy transfer reaction between LSCF and the electrolyte is not rate limiting.[7] We assume this is the case for LSM-YSZ.

3.2.4 Sheet resistance at high cathodic overpotential

Figure 9 shows a typical result for the simulation, using the parameters listed in Table 2 and a cell geometry of 400 μm in current collector width, 400 μm between current collectors and 1 μm in film height, with a cell overpotential of -50 mV. Here we see the basic response for the vacancy distribution (part a) and the potential (part b) in the MIEC film. There is almost zero sheet resistance at this geometry and polarization, as reflected by the nearly equipotential state of the MIEC. The vacancy gradient drives species from the region under the current collector toward the air surface, and from the interface with the electrolyte toward the top surface. The gradient in holes runs in the opposite direction, as dictated by the electroneutrality condition. The flux of holes is not simply opposite to that of vacancies, however; due to their much higher concentration the drift of holes due to the tiny gradients in electrostatic potential counteract the concentration gradient, driving holes toward the current collector.

Figure 10 shows the situation at -750 mV. There is now a significant sheet resistance effect, with the electrostatic potential rising almost 150 mV at the midpoint between current collectors (part b) and the vacancy distribution shows a strong variation, with a precipitous drop occurring at the current collector edge (part a). It is clear that the gradient in vacancies and potential right at the junction is nearly singular, and this is a source of instability at

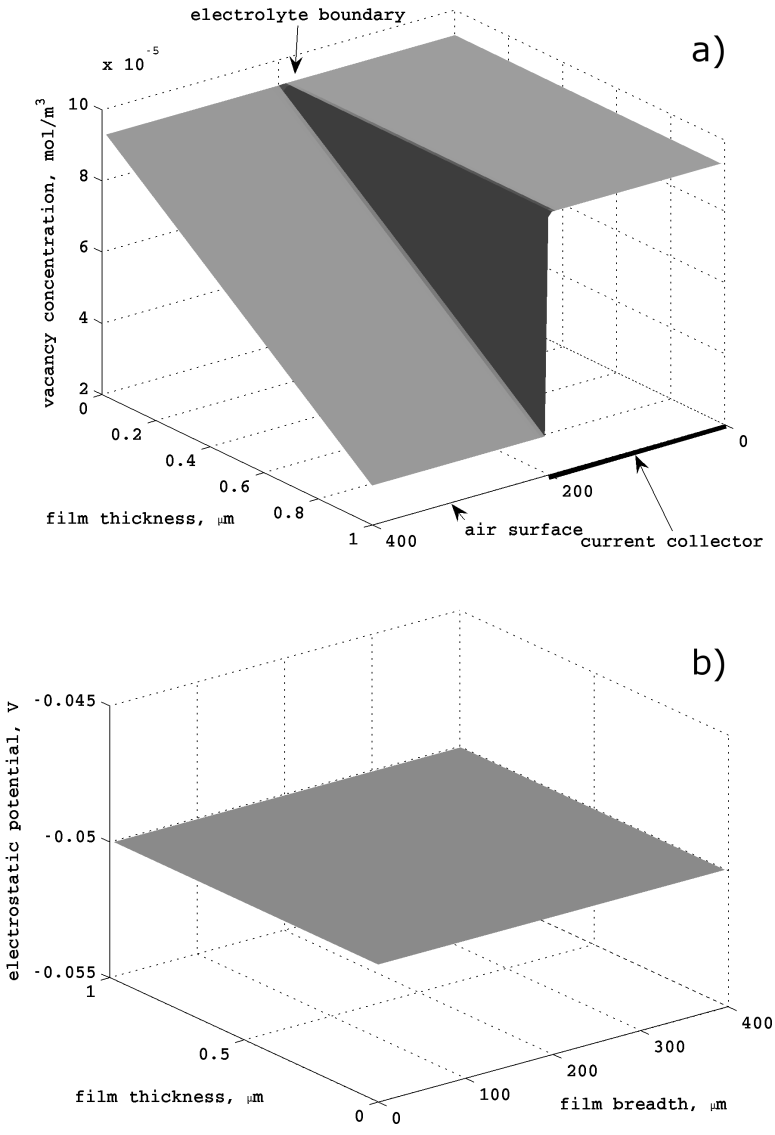

Figure 9: a) Vacancy and b) electrostatic potential distribution for a 1 μm thin film with a 400 μm-wide current collector and 400 μm between current collectors, at -50 mV, using the parameters of Table 2.

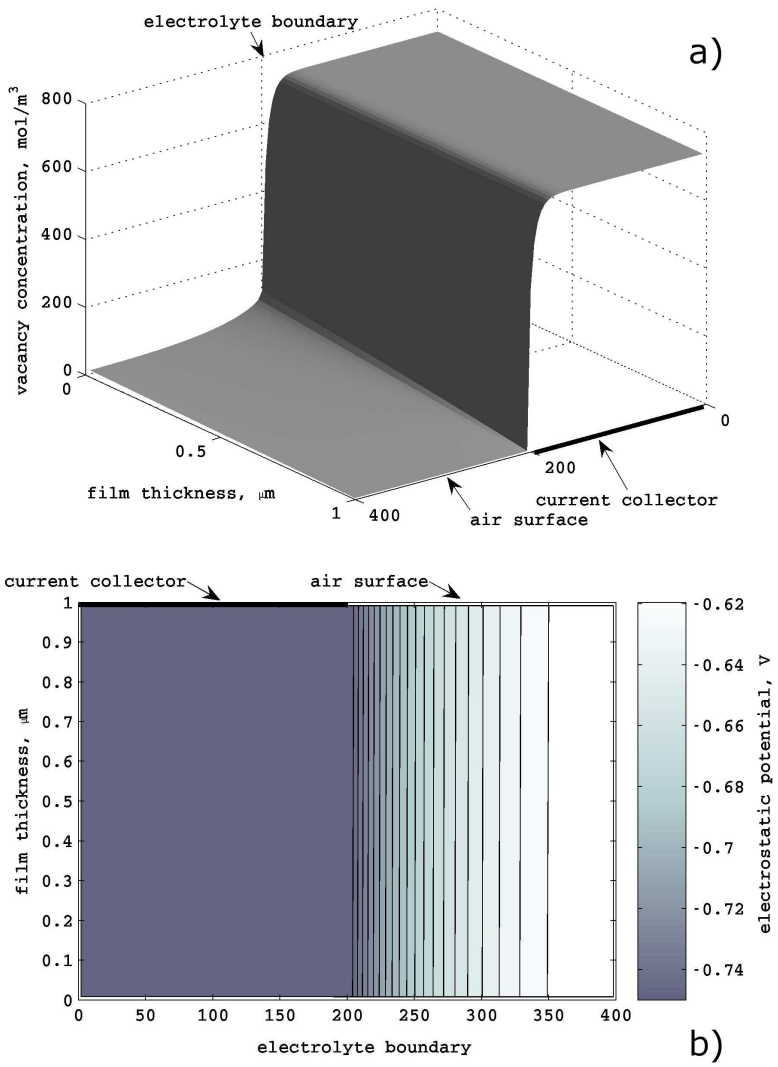

Figure 10: a) Vacancy and b) electrostatic potential (contour plot) for the same film geometry and model parameters as Figure 9, at -750 mV polarization.

even higher cathodic overpotentials.[1] The maximum vacancy concentration underneath the current collector is 736 mol/m^3, which translates to a vacancy site fraction of about 0.028. This is over seven orders of magnitude higher than at equilibrium.

Figure 11 shows a set of I-V curves for films of various thicknesses, from 50 nm up to 1 μm (part a) and the corresponding utilization curves (part b). Here we define *utilization* as the percentage of the potential applied at the current collector attained by the average

[1]Possible cures for this instability are an upwind formulation in the drift term of the flux or a compact scheme. For the purposes of the present analysis, the stability of the current scheme is sufficient.

electrostatic potential in the portion of the MIEC underneath the air-exposed surface. The semi-log I-V plot (part a) shows two straight-line regions, with the slope at high overpotentials shallower than that at low overpotentials. Comparing the two parts of Figure 4 reveals that the change in slope is due to a transition to a sheet resistance-limited regime.

3.2.5 Transport limited at low cathodic overpotential

The straight lines in the semi-log plots suggest a process limited by charge transfer. However, we chose the value of k^0_{v} in Table 2 specifically because we did not want a limiting charge transfer process, and all of the evidence suggests that we succeeded (at least at low overpotentials). Figure 12 shows a set of I-V curves taken at 1 μm thickness with vastly different values for k^0_{v} but with other parameters held to their Table 2 values, with very little change in the film resistance above -500 mV. However, the change in current with the mobility of vacancies (Figure 13) is much more pronounced; the correspondence is almost 1:1. Figure 14 is a log-log plot showing the almost precisely inverse relationship between thickness and current at -5 mV. Actually, the slope is slightly greater than 1, which is likely due to the increasing reduction of the bulk as thicknesses decrease. As cathodic overpotentials increase, the slope of the log-log current-thickness plot also decreases, eventually becoming negative.

Figure 15 shows that in this parameterization, k^0_{inc} is right at the edge of co-limitation with the bulk, as changes of increasing magnitude are seen for a reduction in the parameter but there is virtually no change for increases.

These features – exponential I-V relationship with linear relationship between thickness and resistance – reflect those seen in thin-film experiments and in DC models of mixed conducting cathodes. Our explanation for the behavior is essentially the same as that of Svensson.[98] To say it succinctly, Boltzmann statistics yields an exponential relationship between the extra energy applied to the system and the excess concentration of vacancies which the MIEC may accomodate, in analogy to Hebb-Wagner polarization.[90] However, in our treatment there is no need to break down the overall applied voltage into separate terms as is normally done,[97, 98, 19] since everything is tied up in the single kinetic expression

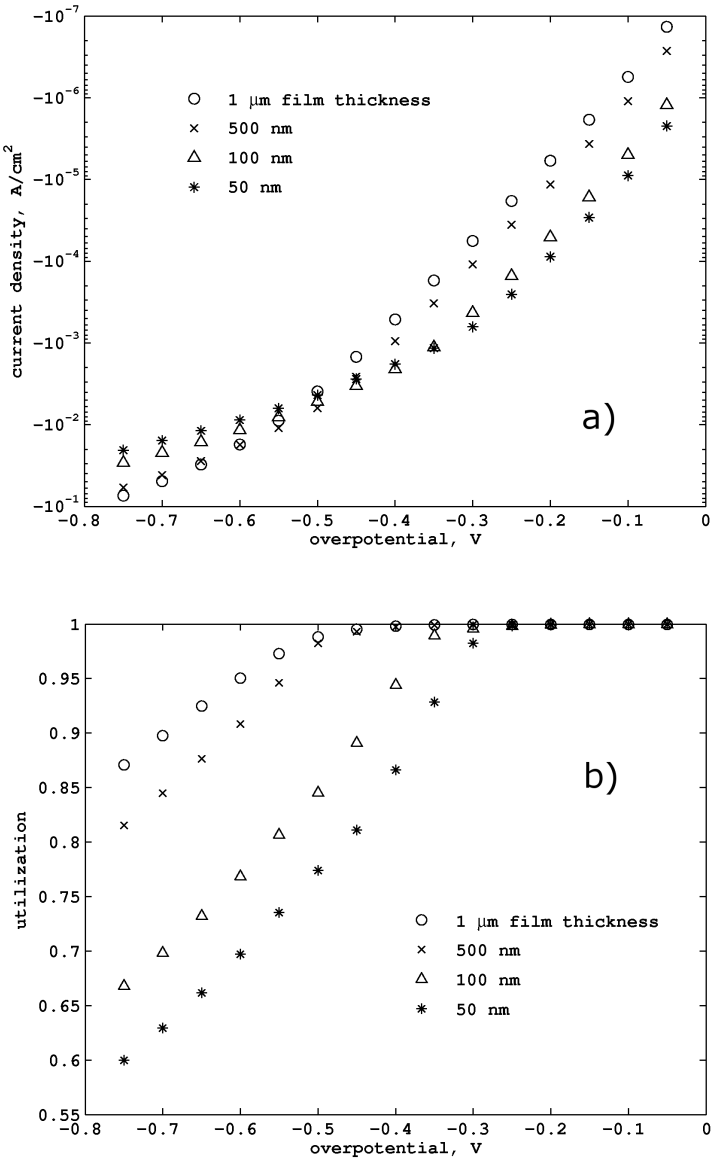

Figure 11: a) I-V curves and b) utilization curves for films of various thicknesses.

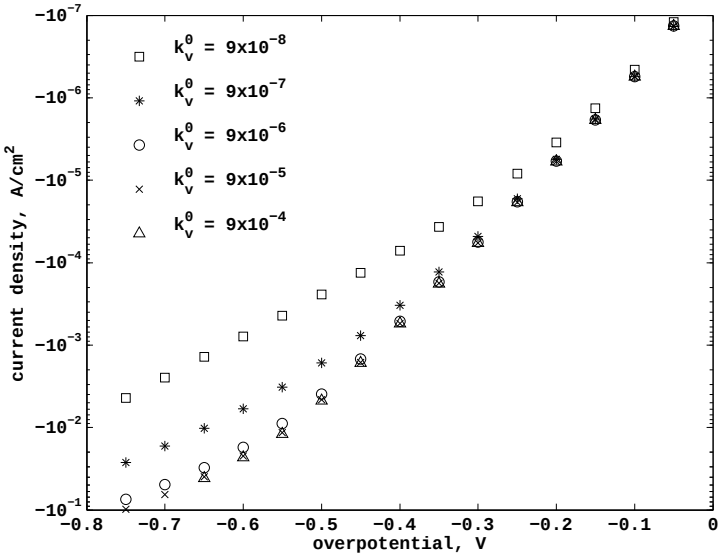

Figure 12: I-V curves for a 1 μm film and various values for the constant k_v^0.

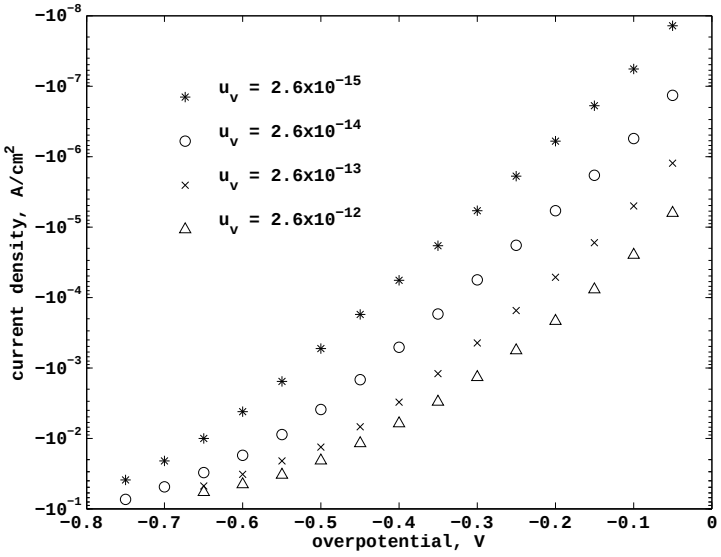

Figure 13: I-V curves for a 1 μm film and various values for the mobility of vacancies, u_v.

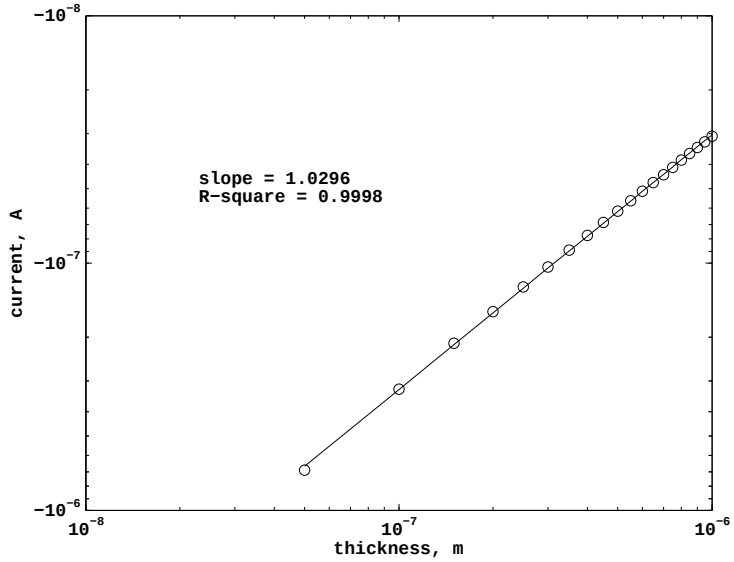

Figure 14: Log-log plot of thickness vs. current for films at -5 mV overpotential.

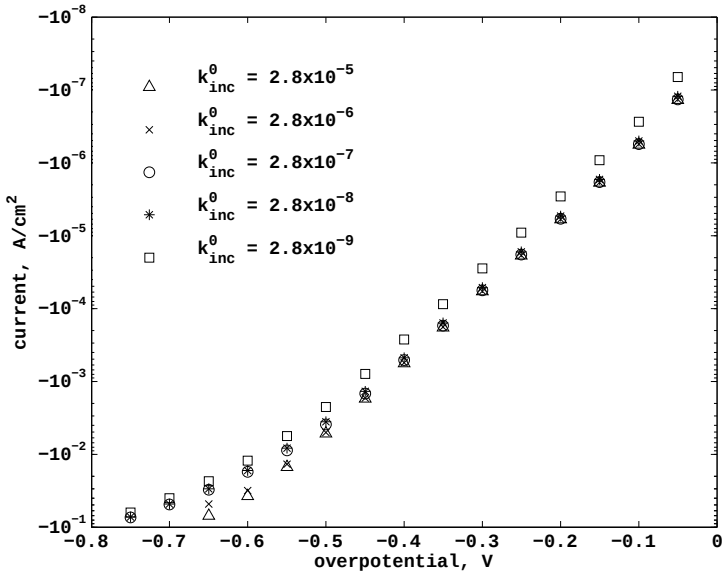

Figure 15: I-V curves for a 1 μm film and various values for the incorporation rate constant, k^0_{inc}.

of Equation (27).

When sheet resistance becomes significant at high overpotentials, the effect is to limit the active area of the film. However, if ionic transport near the current collector is still rate-limiting, current will still respond exponentially to overpotential increases. Therefore the response is another straight-line region in the semi-log plot, albeit with a shallower slope.

3.2.6 Comparison with experimental studies

Since we chose our parameters from the literature based on LSM, we will briefly survey studies featuring LSM thin films. Mizusaki[77] and Ioroi[45, 46] reported on thin LSM films deposited by laser ablation (for Mizusaki) and EVD (for Ioroi). The most striking feature of the comparison between these experiments and the model is the large disagreement on area-specific polarization resistance (ASR) near the limit of zero polarization. Ioroi reports open-circuit ASR on the order of 250 $\Omega{\cdot}cm^2$ for 1.7 μm thick $LaMnO_3$ at 800 °C in air,[45] and Mizusaki reports the same order of magnitude (somewhat lower) for an 0.9 μm $La_{0.63}Sr_{0.27}MnO_{3\pm\delta}$ film at 800 °C. By contrast, the model's ASR for 1 μm thick LSM20 at -5 mV (reflecting 750 °C in air) is 6.5x10^5 $\Omega{\cdot}cm^2$, a difference of over three orders of magnitude.

While several factors may explain the discrepancy, one likely cause is that the experimental films are defective in some unaccounted-for manner. We base this conclusion on more recent results from Imanishi, *et al.*[44] Imanishi and co-workers developed a method for producing epitaxial films of LSC on YSZ substrates (see also Mori, *et al.*[80]). Epitaxial or near-epitaxial films are much less likely to contain nanoporosity, and by definition contain fewer grain boundaries. The DC-measured, electrolyte compensated current for Imanishi's 30 nm LSM20 film deposited on the YSZ (110) surface at approximately -17 mV, 0.1 atm P_{O_2} and 700 °C was -10^{-5} $A{\cdot}cm^{-2}$, whereas that of our model at the same thickness and polarization at 750 °C is -7.4x10^{-7} $A{\cdot}cm^{-2}$ – still over an order of magnitude lower, but notably, much closer than the earlier experiments. At higher overpotentials, the difference narrows even more: Imanishi reports -10^{-4} $A{\cdot}cm^{-2}$ at approximately -109 mV, whereas the

simulation gives -1.6x10^{-5} A·cm^{-2}.

Qualitatively, the shape of Imanishi's I-V curves are consistent with the shape of the curves in Figure 11, displaying two plausibly linear regimes on the semilog scale separated by a transition region. I-V curves reported by Mizusaki and Endo[27] display similar shapes.

The remaining difference in ASR between Imanishi and the model is probably due (in large part) to incorrect values for diffusivity, equilibrium vacancy concentration, incorporation rate constant or a combination. It seems otherwise unlikely that the model's approximations (at low overpotential, these chiefly pertain to the surface model) would make an order of magnitude difference. The narrowing of the difference at high overpotentials further corroborate the idea that Imanishi's experiments encounter a sheet resistance effect.

3.2.7 Implications

The favorable comparisons between the behavior of the model and the experimental systems suggest that these thin film experiments are encountering sheet resistance at overpotentials common to operating fuel cells. Although it is difficult at this point to provide quantitative guidance, it should be pointed out that in experiments where the thickness of the LSM electrode falls below 1 μm, there may be sheet resistance to contend with. This is the case for patterned electrodes, thin films or porous electrodes. Especially in the case of nanostructuring, it would seem prudent to take current collection into account when designing new electrode architectures.

3.3 Incorporation of a triple-phase boundary

Matt Lynch has taken the lead in deriving and implementing a model that incorporates a TPB reaction. The model geometry is similar to that shown in Figure 6b), but with an opening in the LSM film as depicted in Figure 7b). Mr. Lynch derived a rate expression for the reaction at the TPB (wherein an adsorbed oxygen combines directly with a vacancy in YSZ) under the same principles discussed in chapter 2. Mr. Lynch also derived a method for incorporating surface diffusion of species. Results of the simulation appear in Figure 16, which shows the division of current between the surface and bulk pathways as a function of thickness and TPB reaction rate, and 17, which shows the thickness-dependent behavior

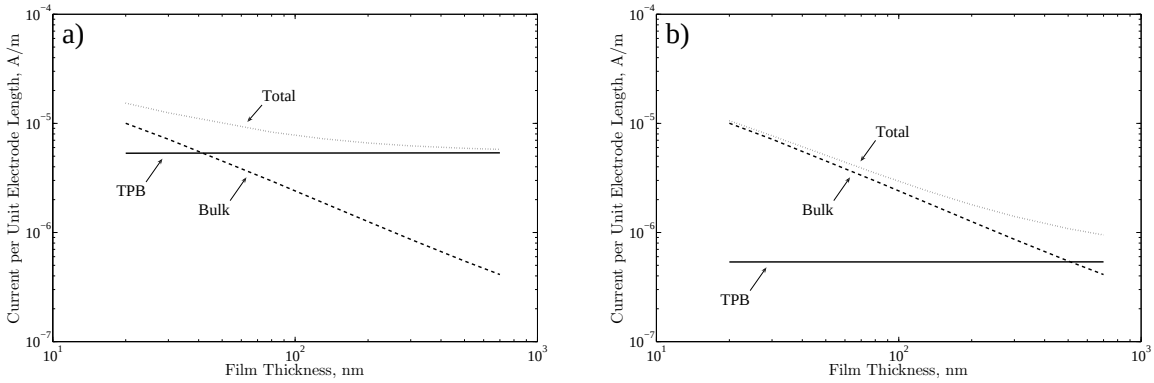

Figure 16: Division of current between surface and bulk pathways for the patterned electrode model with TPB, for two different TPB reaction rates and overpotential of -0.1 V. Figure produced by Matt Lynch.

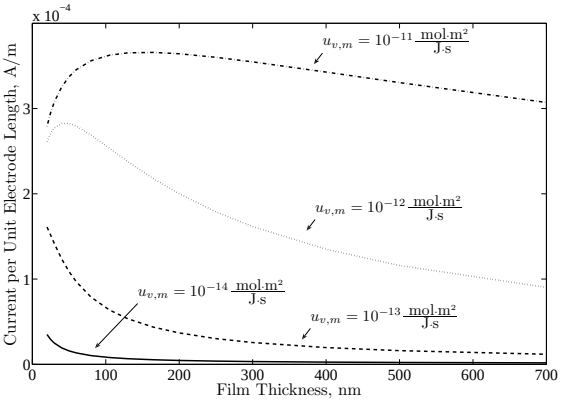

Figure 17: Dependence of current on thickness in the patterned electrode model with TPB for several different oxygen vacancy mobilities. Applied overpotential is -0.1 V. Figure produced by Matt Lynch.

for films with different vacancy mobilities. Both results reflect the qualitative behavior of thin film and patterned electrode experiments. In particular, Figure 17 replicates the thickness-dependent critical behavior seen in patterned electrodes and attributable to sheet resistance.[60]

CHAPTER IV

REFINEMENT OF THE BULK DEFECT MODEL FOR 20% STRONTIUM-DOPED LSM

4.1 Introduction

Toward the overall goal of a better quantitative understanding of LSM, one of the first challenges is an accurate understanding of the bulk defect structure. The behavior of bulk defects in LSM are experimentally accessible through gravimetry and wet chemical methods (such as iodometry), and the defects themselves are directly observable through TEM and neutron diffraction. The principal difficulty is that oxygen defects, which are crucial to LSM's behavior as a mixed ionic-electronic conductor, are very rare in LSM at near-atmospheric partial pressures of oxygen and low cathodic overpotentials. This means that direct measurement of the oxygen defect concentration at near-atmospheric pressures is extremely difficult; it can only be indirectly calculated through a thermodynamic model.

The search for such a model for LSM is now decades old, and the principal tool in its development is the nonstoichiometry experiment, wherein a powder sample on a precision balance is brought to a certain temperature and exposed to various partial pressures of oxygen. The weight change can be converted into changes in the oxygen stoichiometry. Early measurements by Kamata[52] were followed by a more in-depth study by Kuo and Anderson.[64] Since then, several authors have made additional measurements (a difficult undertaking, especially for the very low oxygen pressures required to obtain significant oxygen deficiency in LSM) or contributed analysis of the data.[101, 105, 103, 104, 78, 76, 82, 88, 112]

Poulsen [88] devised a flexible random defects model that can be viewed as the culmination of years of experimental observation and theoretical development by various authors, and applied it to Kuo and Anderson's nonstoichiometry data as well as conductivity data.[63] The ability of the model to replicate nonstoichiometry data was very good, while

the fit to conductivity data was less accurate.

Our initial goal was to use Poulsen's model straightforwardly to estimate defect reaction equilibrium constants at temperatures and compositions of interest to us, while perhaps improving somewhat on Poulsen's mathematical solution technique in order to obtain a more accurate and verifiable parameter estimate. However, we found that a completely random model inadequately described the behavior of the samples at low temperatures. This led us to modify the random theory slightly, in order to account for cation defect interactions. This resulted in a significant improvement in both the fit to nonstoichiometry and perhaps to conductivity data.

4.2 Inverse Problem Techniques

This crucial element of the entire program of study was developed, tested and successfully implemented in the course of this work. We chose a particle swarm optimizer (PSO) as the optimization tool, and developed a rigorous method of determining local identifiability.

4.2.1 Particle swarm optimizer

The most important part of the mathematical analysis is the optimizer. We sought a robust optimizer, proven effective in finding global optima in a complex, multidimensional search space. Non-gradient methods such as evolutionary and genetic algorithms are the best candidates, and of these perhaps the best (and simplest) is the particle swarm optimizer.

The PSO was first devised by behavioral scientists to model the flocking behavior of birds, but the inventors quickly realized that they had found a powerful method of computational optimization.[55] The basic principle is that a number of agents, each representing a point in parameter space, move about the space with a velocity influenced by the best positions found by its neighbors. Using the notation of Mendes, *et al.* [73], the process of

updating the position of each agent at each iteration may be written:

$$\phi_k = U\left[0, \frac{\phi_{max}}{\|\mathcal{N}\|}\right] \quad \forall k \in \mathcal{N} \tag{31a}$$

$$\overrightarrow{P}_m = \frac{\sum_k \phi_k \overrightarrow{P}_k}{\sum_k \phi_k} \tag{31b}$$

$$\overrightarrow{v}_{t+1} = \chi\left[\overrightarrow{v}_t + \left(\overrightarrow{P}_m - \overrightarrow{X}_t\right)\sum_k \phi_k\right] \tag{31c}$$

$$\overrightarrow{X}_{t+1} = \overrightarrow{X}_t + \overrightarrow{v}_{t+1} \tag{31d}$$

where $\mathcal{N}$ is the set of all agents in the neighborhood of the agent being updated, $U[a, b]$ is an operator returning a random number between a and b, $\overrightarrow{P}_k$ is the best position found by agent k, $\overrightarrow{v}$ is the agent's velocity and $\overrightarrow{X}$ its position. χ and ϕ_{max} are constants that must take particular, theoretically-derived values in order to encourage convergence.[18]

Mendes, *et al.*[73] introduced the idea of using the best positions of all the agents in a predetermined neighborhood in the update process, instead of merely the best agent, and also tested several different topologies for determining each agent's neighborhood. The most reliable topology for a series of test runs was what Mendes called the "unselfed ring" topology, wherein an agent's neighborhood consists of its two nearest neighbors, but not itself. This is the topology we used in the following analysis.

4.2.2 Identification

It is well known in the discipline of parameter estimation that care must be taken in complex problems to ensure that results are unique. That is, one must ensure that the optimum does not occur at a saddle point. For linear problems, there may be methods to determine global identifiability of a model *a priori*. However, for nonlinear problems of the type we are likely to encounter, it is only possible to examine local identifiability *a posteriori*.

The method we chose is an analysis of the behavior of each individual misfit, or the difference between each data point and the corresponding model output, with respect to changes in the parameters.[15] (The sum of the squares of the misfits is the cost, or the

function to be optimized.) One computes a rectangular matrix J via the following:

$$\eta : \mathbb{R}^P \to \mathbb{R}^N, \quad N > P \tag{32a}$$

$$J(\alpha) = \nabla\eta(\alpha) \tag{32b}$$

where η is the mapping from parameter space into the output space represented by the model, P is the number of parameters, N is the number of output data points, and α is the optimum parameter set. We compute partial derivatives by finite difference, using a highly accurate algorithm involving complex numbers.[37] The matrix J has dimensions NxP. The test for local identifiability at α is whether the columns of J are linearly independent.

Here we encounter the problem that, in a system with model, experimental and computational errors, we will never encounter a truly linearly dependent set of vectors. We must therefore devise methods for analyzing the proximity to linear dependence of this vector set, along with standards to apply to the results. The method we developed here takes the form of a constrained minimization:

$$\min\|Jx\|^2 \tag{33a}$$

$$\|x\|^2 = \beta, \quad \beta > 0 \tag{33b}$$

Solving with Lagrange multipliers,

$$\begin{gathered} J^T Jx + \lambda x = 0 \\ x^T x = \beta \end{gathered} \tag{34a}$$

$$\Rightarrow \quad x^T J^T Jx = -\lambda x^T x = -\lambda\beta \tag{34b}$$

So the size of the eigenvalue indicates the proximity of the corresponding eigenvector x to the nullspace of J, with the lowest eigenvalue corresponding to the direction in parameter space x along which there is the lowest change in the cost function.

A more precise proof:

$$\|\eta(\alpha + sx) - \eta(\alpha)\| = sJx + \mathcal{O}(s^2) \tag{35a}$$

with $\|x\| = 1$ and s a scalar. Therefore,

$$\|\eta(\alpha + sx) - \eta(\alpha)\|^2 = s^2 x^T J^T Jx + \mathcal{O}(s^4) \tag{35b}$$

Let λ_i and r_i, $i \in [1, P]$ be the eigenvalues and eigenvectors, respectively, of $J^T J$. Since $J^T J$ is symmetric, r_i is an orthonormal set. Therefore

$$x = \sum_i c_i r_i \tag{35c}$$

$$x^T J^T J x = \sum_i c_i^2 \lambda_i \geqq \lambda_0 \tag{35d}$$

with λ_0 the smallest eigenvalue. Therefore, by (35b), for any fixed perturbation s which is small enough, $\|\eta(\alpha + sx) - \eta(\alpha)\|$ finds a minimum at $x = r_0$.

With the direction of smallest change identified, we may easily produce a cost contour along this direction, looking at the change in the least sensitive parameter versus the change in the cost. The threshold we used is a ratio of the latter to the former of 0.2 over a 5% total change in the least sensitive parameter. A ratio any less than this is considered non-unique in the affected parameter.

4.3 Random Model

4.3.1 Model review

Following Poulsen [88], the random defect model is

$$\text{Schottky:} \qquad \mathsf{nil} \rightleftharpoons 3\mathsf{V}_{\mathsf{O}}^{\cdot\cdot} + \mathsf{V}_{\mathsf{B}}^{\prime\prime\prime} + \mathsf{V}_{\mathsf{A}}^{\prime\prime\prime} \tag{36a}$$

$$\text{Reduction:} \qquad \frac{1}{2}\mathsf{O}_2 + 2\mathsf{Mn}_{\mathsf{B}}^{\mathsf{x}} + \mathsf{V}_{\mathsf{O}}^{\cdot\cdot} \rightleftharpoons \mathsf{O}_{\mathsf{O}}^{\mathsf{x}} + 2\mathsf{Mn}_{\mathsf{B}}^{\cdot} \tag{36b}$$

$$\text{Disproportionation:} \qquad 2\mathsf{Mn}_{\mathsf{B}}^{\mathsf{x}} \rightleftharpoons \mathsf{Mn}_{\mathsf{B}}^{\prime} + \mathsf{Mn}_{\mathsf{B}}^{\cdot} \tag{36c}$$

leading to

$$\kappa_s = [\mathsf{V}_{\mathsf{A}}^{\prime\prime\prime}][\mathsf{V}_{\mathsf{B}}^{\prime\prime\prime}][\mathsf{V}_{\mathsf{O}}^{\cdot\cdot}]^3 \tag{37a}$$

$$\kappa_r = \frac{[\mathsf{Mn}_{\mathsf{B}}^{\cdot}]^2(1 - [\mathsf{V}_{\mathsf{O}}^{\cdot\cdot}])}{(1 - [\mathsf{Mn}_{\mathsf{B}}^{\cdot}] - [\mathsf{Mn}_{\mathsf{B}}^{\prime}] - [\mathsf{V}_{\mathsf{B}}^{\prime\prime\prime}])^2 [\mathsf{V}_{\mathsf{O}}^{\cdot\cdot}] \mathsf{pO_2}^{1/2}} \tag{37b}$$

$$\kappa_d = \frac{[\mathsf{Mn}_{\mathsf{B}}^{\prime}][\mathsf{Mn}_{\mathsf{B}}^{\cdot}]}{(1 - [\mathsf{Mn}_{\mathsf{B}}^{\cdot}] - [\mathsf{Mn}_{\mathsf{B}}^{\prime}] - [\mathsf{V}_{\mathsf{B}}^{\prime\prime\prime}])^2} \tag{37c}$$

$$r_A = \frac{1 - [\mathsf{Sr}_{\mathsf{A}}^{\prime}] - [\mathsf{V}_{\mathsf{A}}^{\prime\prime\prime}]}{[\mathsf{Sr}_{\mathsf{A}}^{\prime}]} \tag{37d}$$

$$r_B = \frac{1 - [\mathsf{V}_{\mathsf{A}}^{\prime\prime\prime}]}{1 - [\mathsf{V}_{\mathsf{B}}^{\prime\prime\prime}]} \tag{37e}$$

$$0 = 6[\mathsf{V}_{\mathsf{O}}^{\cdot\cdot}] + [\mathsf{Mn}_{\mathsf{B}}^{\cdot}] - 3[\mathsf{V}_{\mathsf{A}}^{\prime\prime\prime}] - 3[\mathsf{V}_{\mathsf{B}}^{\prime\prime\prime}] - [\mathsf{Sr}_{\mathsf{A}}^{\prime}] - [\mathsf{Mn}_{\mathsf{B}}^{\prime}] \tag{37f}$$

where r_A and r_B are the cation ratios of lanthanum to strontium and total A-site cations to manganese, respectively. The mass-action expressions are a result of rigorous derivation of the configurational entropy, taking site restrictions into account and assuming no defect interaction. Given the equilibrium constants and cation ratios, this is a system of 6 equations and 6 unknowns. Poulsen solved the system using a searching procedure based on a range of possible values for $[V_O^{\cdot\cdot}]$. We augmented this method by using a Newton solver to find the final solution, using the best result from the searching procedure as an initial guess.

4.3.2 Data selection

In this work we have used nonstoichiometry data gathered by Mizusaki, *et al.*[76] One reason for this is that we are interested in relatively low temperatures, and Mizusaki's experiments covered a temperature range of interest, from 873 to 1273K. Another reason is that Mizusaki corrected for the changes in the buoyancy of the atmosphere by subtracting the weight change of an alumina sample subjected to the same atmosphere and temperature. This approach seems to make a significant difference, as there is a noticeable divergence between Kuo's results and Mizusaki's at 1273K (the only temperature for which the two overlap), especially at low oxygen pressures. The best fit of Poulsen's model to Mizusaki's data for 20% Sr-doping is almost five times better (per data point) than the best fit of the same model to Kuo's measurements at the same composition and temperature (see Figure 18).

4.3.3 Results

Fits to the data for $La_{0.8}Sr_{0.2}MnO_{3\pm\delta}$ (LSM20) are found in Figure 19. The fit to low-pressure data are generally quite good except at 873K. At high pressures, however, the experimental data is not captured by the model very well, with an increasing separation as temperature decreases. The experimental increase in stoichiometry is suppressed compared to that of the model. At 873K, the model completely fails to replicate the data, even at the low-pressure end.

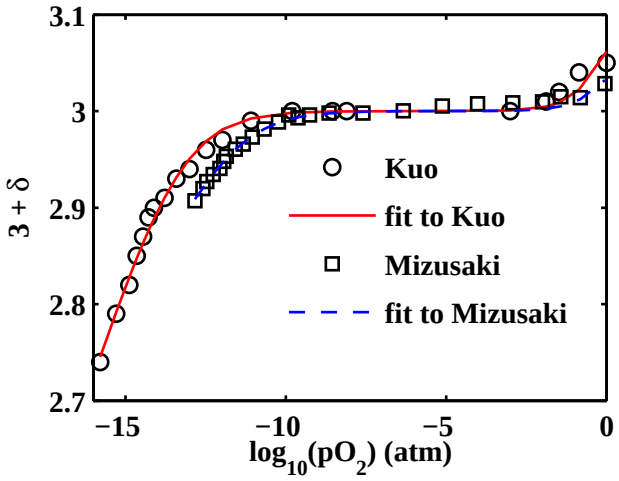

Figure 18: Comparison between Mizusaki's measurements and Kuo's for $La_{0.8}Sr_{0.2}MnO_{3\pm\delta}$ at 1273K.

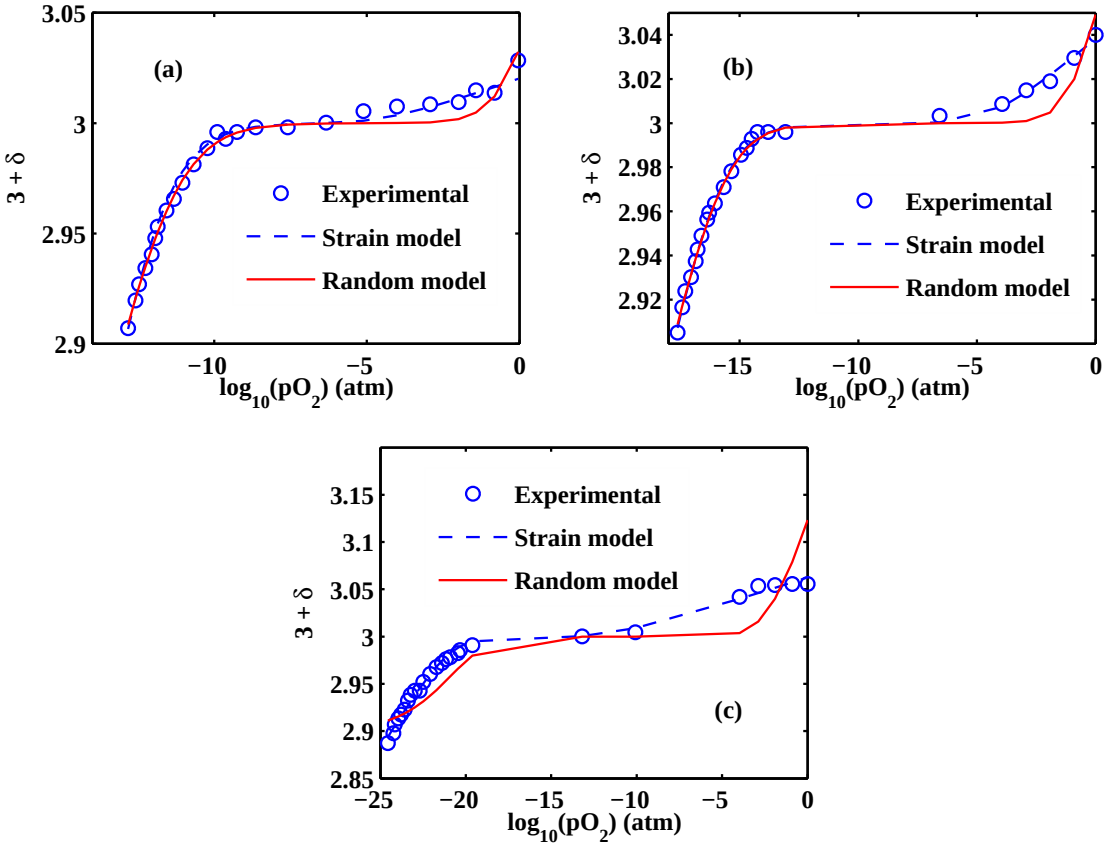

Figure 19: Fits to experimental data of ref. [76] for LSM20, at (a) 1273K (b) 1073K and (c) 873K.

4.4 Strain model

4.4.1 Rationale and derivation

The suppression of oxygen stoichiometry at high-pressures and low temperatures was pointed out by Mizusaki.[76] It was also clearly reflected in the data of vanRoosmalen and Cordfunke for samples with zero Sr content.[103] Since oxygen is added through the creation of new sites via the Schottky reaction, these results indicate either a shifting of the equilibrium of the Schottky reaction (36a) toward the perfect crystal as pressures increase, or a shifting of the equilibrium in the reduction reaction (36b) toward the gas.

A suppression of the oxygen vacancy concentration through a clustering reaction could cause the latter, but vanRoosmalen, *et al.* [105] found no evidence of defect clustering or small-scale phase changes in LSM using HRTEM. This suggests that an interaction between cation defects is behind the behavior. Given that the excess free energy we seek is positive, and that relatively large strain fields can be expected to develop around the trivalent cation vacancies, it seems likely that the source of the excess free energy is a strain interaction between cation defects.

The excess free energy due to strain field interaction between crystal defects is quadratic in the concentration of the defect, leading to an excess term in the chemical potential proportional to the concentration.[68] Considering vacancies on the A and B sites to be the only defects for which the strain effect is considerable, and further assuming an equal strain due to each type of defect, leads to a re-writing of the mass-action law for Schottky equilibrium:

$$\kappa_s \exp\left[\frac{-\gamma([\mathsf{V}_\mathsf{A}'''] + [\mathsf{V}_\mathsf{B}'''])}{RT}\right] = [\mathsf{V}_\mathsf{A}'''][\mathsf{V}_\mathsf{B}'''][\mathsf{V}_\mathsf{O}^{\cdot\cdot}]^3 \tag{38}$$

where γ is a constant depending on the average elastic constant of the material and the amount of strain imparted by each new defect.

The basic solution methodology remains the same for this model as for the random model – a search through candidate values for $[\mathsf{V}_\mathsf{O}^{\cdot\cdot}]$ followed by Newton's method.

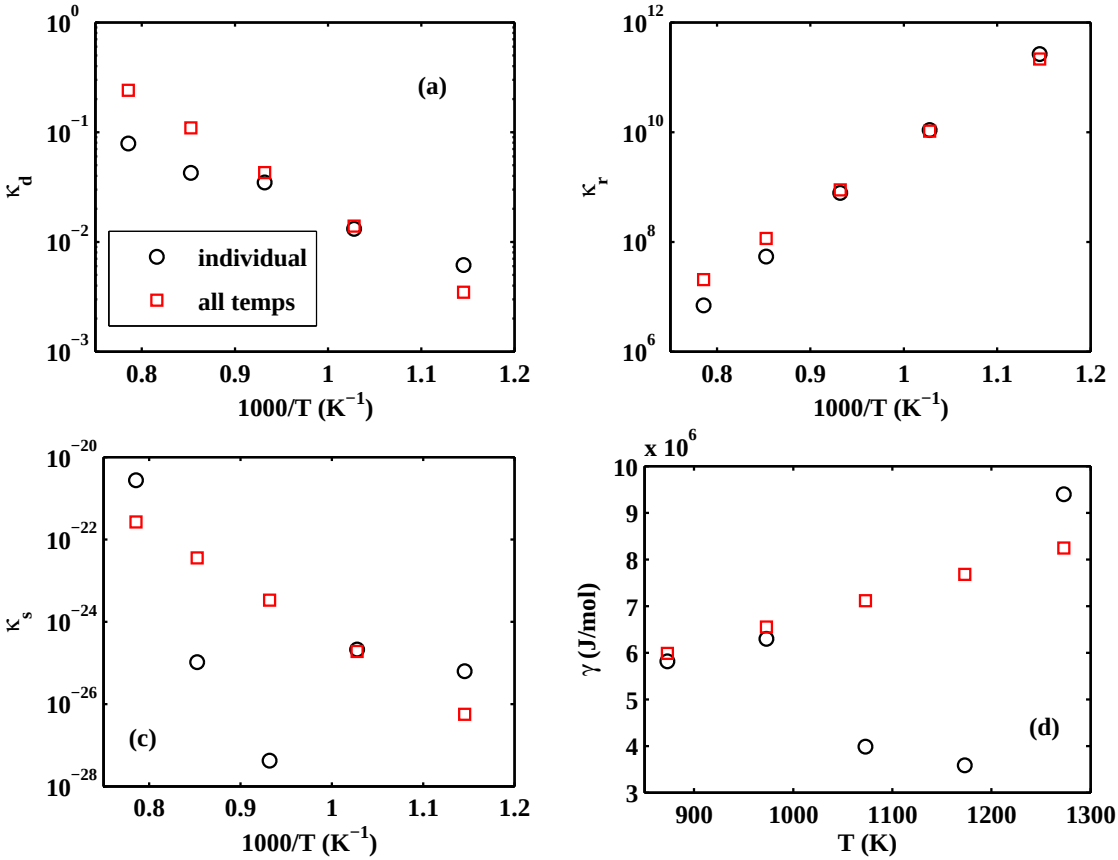

Figure 20: Parameters found by fitting the strain model to data for LSM20 at each temperature individually, and for all temperatures together. The parameters are (a) κ_d (disproportionation) (b) κ_r (reduction) (c) κ_s (Schottky) (d) γ (strain coefficient).

4.4.2 Results and discussion

Fits of the strain model to the data for LSM20 show a distinguishably better fit than for the random model at all temperatures (see Figure 19). The improvement increases as temperature drops, since the effect of strain interaction becomes more significant at lower temperatures. It is clear that the model suitably represents the data at 873K.

To estimate activation energy and vibrational entropy for the three equilibrium constants, we created Arrhenius plots. We also plotted the parameter γ vs. temperature (see Figure 20). Notably, while the data for reduction and disproportionation constants fall more or less on a straight line, the data for Schottky equilibrium and strain interaction are erratic.

A look at the local identifiability for these fits reveals the likely culprit for the erratic

behavior in the Schottky constant: it is by far the least sensitive of all the parameters in the area of the optimum at each temperature, and the analysis described above reveals that each of these fits fails the test of identifiability. At 1273K, for instance, κ_s may change more than 5% while the cost function changes less than 0.01%.[1] This means that the data gathered in a single nonstoichiometry experiment is insufficent to uniquely determine the constants in this model.

We solve this problem, however, if we take advantage of the power of the optimizer to fit this model to all of the temperatures at once. We do this by using the activation energy and vibrational entropy for each defect reaction as parameters, and by requiring the values for γ also to fall on a straight line. This is an eight-parameter optimization problem, reduding the ratio of parameters to data points by more than half.

One test of the validity of this procedure is whether or not the fitted result continues to outperform the random model. Figure 21, a comparison of optimum cost functions at each temperature, shows that it does. As for uniqueness, as expected, the behavior is much more stable. Figure 22 shows a plot of the change in the least sensitive parameter (the vibrational entropy for the Schottky reaction) along the least sensitive direction in parameter space at the optimum. It clearly exceeds our standard.

Table 3 lists the optimized constants for LSM20, while Table 4 lists parameters for $La_{0.9}Sr_{0.1}MnO_{3\pm\delta}$ (LSM10). The constants for LSM10 were also found through the all-temperature approach, leading to a consistently better fit than the random model and an acceptable degree of uniqueness. (See Figure 22. The change in the overall cost is less than that for LSM20, most likely due to noisier data, but it still well exceeds the standard.) The disproportionation reaction changes from a positive activation energy with positive vibrational entropy in LSM20 to the opposite in LSM10, but Nowotny and Rekas reported similar behavior.[82] Also, for LSM20 the strain coefficient goes up slightly with temperature, whereas in LSM10 the trend is reversed. One expects that this parameter should decrease slightly with temperature, as both the elastic modulus and the average strain induced by a defect will likely decrease (albeit slightly) as temperatures go up. The

[1] The random model is closer to identifiable, but still fails the standard at 1273K.

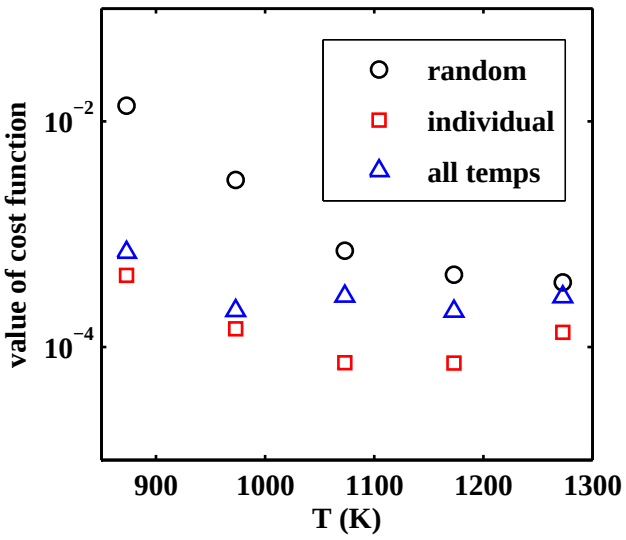

Figure 21: Comparison of cost values for the fit to data of ref. [76] using the random model, the strain model fit individually to each temperature, and the strain model fit to all temperatures at once.

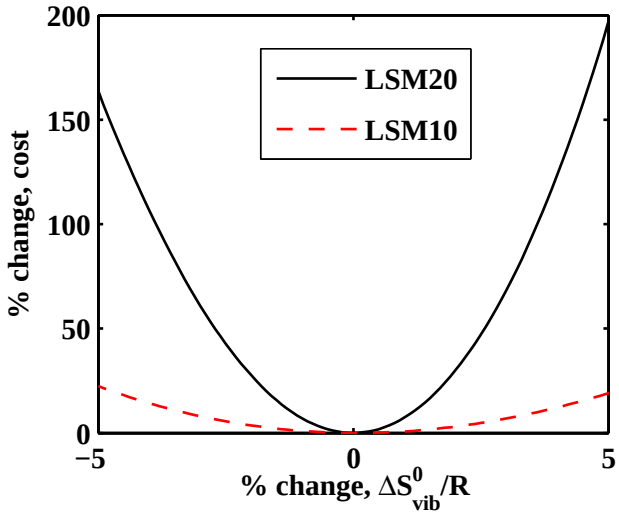

Figure 22: The change in the cost along the least sensitive direction, with respect to the least sensitive parameter (ΔS^0_{vib} for the Schottky reaction) for all-temperature strain model fits to LSM20 and LSM10 data from ref. [76].

Table 3: Parameters for LSM20

	κ_d	κ_r	κ_s	γ
-$\Delta H^0/R$, K (slope)	-1.18 x10^4	2.57 x10^4	-2.99 x10^4	1.09x10^4 J/mol·K
$\Delta S^0_{\text{vib}}/R$ (intercept)	7.82	-3.36	-26.2	-4.23x10^6 J/mol

Table 4: Parameters for LSM10

	κ_d	κ_r	κ_s	γ
-$\Delta H^0/R$, K (slope)	1.96 x10^3	4.24 x10^4	-6.30 x10^4	-7.35x10^2 J/mol·K
$\Delta S^0_{\text{vib}}/R$ (intercept)	-2.43	-14.5	-8.01	2.91x10^6 J/mol

fact that there is an increase with temperature in LSM20 suggests that there may still be some interaction effect not accounted for; perhaps strain due to some other defect or an electrical interaction.

Poulsen's fit to conductivity models was somewhat problematic, since the random model (fit to Kuo's data) predicts a sharp increase in the availability of mobile electronic charge carriers in the superstoichiometric region [88], where conductivity measurements show no change.[63, 79] We did not fit the results to conductivity data in order to estimate mobilities; however, the Kröger-Vink plots of Figure 23 reveal an interesting result. The strain model shows less change in the total Mn(IV) concentration at high pressures. The total charge carrier concentration on the B-site shows a similar profile, with the strain model closest to the optimum carrier-to-site ratio of 0.5.

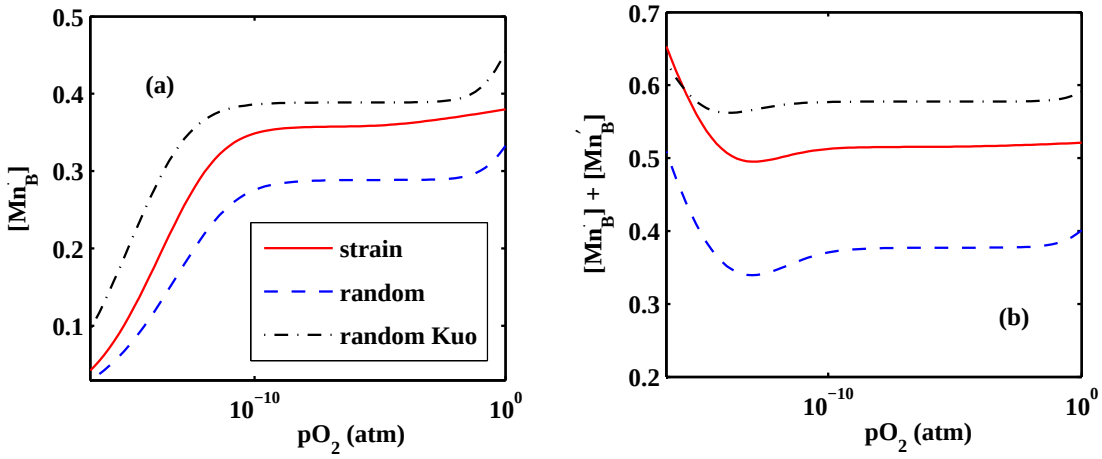

Figure 23: (a) Mn(IV) and (b) Mn(IV) + Mn(II) concentrations for various models fit to nonstoichiometry data at 1273K.

CHAPTER V

TOWARD BUILDING A MODEL AND TESTING REGIME FOR THE LSM-YSZ INTERFACE

5.1 Blocked electrodes

The best experimental vehicle for isolating the processes at the LSM-YSZ interface and determining its structure is a blocked electrode (see Figure 24). In the blocked electrode experiment, a dense film of LSM is deposited on a YSZ substrate, followed by a dense layer of Pt. A porous Ag counter electrode is applied to YSZ, and the capacitance of the entire structure is measured for a variety of different terminal potentials. The capacitance at the counter electrode, being a free surface for the transport of oxygen, should contribute little to the capacitance compared with the LSM-YSZ and LSM-Pt interfaces. In any event, for a truly sealed system, it should be possible to estimate polarizations at the Pt-YSZ and Ag-YSZ interfaces using potentiometry. Such an experimental cell design has been used to study the structure of the interface between YSZ and Pt.[16, 40, 100]

The characterization method for the blocked electrode experiments is impedance spectroscopy (IS) under applied bias. IS is the application of a small-signal A/C voltage perturbation through several decades of frequency (typically mHz to MHz range). For the equilibrium case, we are interested only in the behavior of the low-frequency capacitance with respect applied potential. We can analyze the frequency-dependent behavior using the nonequilibrium model described below.

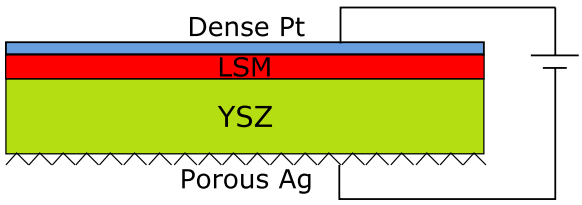

Figure 24: Schematic of the blocked electrode test cell

5.2 Theory

5.2.1 Randomly distributed mobile defects

A naive approach to modeling the interface – one concordant with the assumption of a random distribution of defects in both YSZ and LSM – is the solution of the Poisson-Fermi equation with Dirichlet boundary conditions at the current collectors and a partition in the domain at the LSM-YSZ boundary. Such a problem has been derived and solved using adaptive finite elements (a discretization scheme which is identical to a finite difference scheme for elliptic equations in one dimension for a regular mesh, but not for an irregular mesh as required in adaptive meshing).

Poisson's equation is:

$$\frac{d^2\phi}{d\xi^2} = -\frac{\rho(\xi)}{\kappa\epsilon_0} \tag{39}$$

where ϕ is the electrostatic potential, acting over a one-dimensional domain $\xi \in [0, L]$, ρ is the excess charge, κ is the dielectric constant of the medium and ϵ_0 is the permittivity of free space required by the SI system of units. Both κ and ρ are discontinuous at the interface, leading to a split in the overall domain. The boundary conditions at the interface are defined by the continuity of the dielectric displacement:

$$\kappa_{\mathrm{YSZ}} \frac{d\phi}{d\xi}|_{\mathrm{YSZ,int}} = \kappa_{\mathrm{LSM}} \frac{d\phi}{d\xi}|_{\mathrm{LSM,int}} \tag{40}$$

where the subscript "int" indicates the interface. The Galerkin finite element discretization, for an indexing starting just off the boundary for ϕ is:

$$-\frac{\phi_{i-1}}{\Delta\xi_i} + \frac{\phi_i}{\Delta\xi_i} + \frac{\phi_i}{\Delta\xi_{i+1}} - \frac{\phi_{i+1}}{\Delta\xi_{i+1}} - \frac{\rho_i}{2\kappa\epsilon_0}\left(\Delta\xi_i + \Delta\xi_{i+1}\right) = 0 \tag{41}$$

where the source term was calculated using trapezoidal quadrature.

The expression for ρ is generally dependent on ϕ, although the particular form depends on the defect equilibrium. It arises from the condition for eqilibrium in the bulk domain, that is, $\nabla\bar{\mu}_j = 0 \quad \forall j$, where j indicates each mobile species. Considering randomly distributed, mobile oxygen vacancies in YSZ, with static, randomly distributed dopant cations, we may write:

$$\frac{[\mathrm{V}_{\mathrm{O}}^{\cdot\cdot}]}{1-[\mathrm{V}_{\mathrm{O}}^{\cdot\cdot}]} = \frac{[\mathrm{V}_{\mathrm{O}}^{\cdot\cdot}]_0}{1-[\mathrm{V}_{\mathrm{O}}^{\cdot\cdot}]_0} \exp\left[\frac{-2F(\phi-\phi_0)}{RT}\right] \tag{42}$$

The reference potential and site fraction are constants that may be solved for by writing chemical equilibrium equations at the boundaries (these involve equilibrium constants that can be directly estimated using potentiometry, as mentioned above), yielding potential-dependent expressions for ρ in the electrolyte.

In LSM, the defect equilibrium is more complicated, as discussed in chapter 4. However, we may still assume a fixed concentration profile of metal vacancies and dopant ions. This leads to a potential-dependent system of equations for the mobile defect site fractions at each point. It is a differentiable system, so it can be used in the calculation of the Jacobian required for Newton's method.

Newton's method is used for the solution. The Jacobian in this case is tri-diagonal, so the complexity in the solver is $\mathcal{O}(N)$.

Typical results are displayed in Figure 25, for the case of cathodic applied potential to the working electrode (LSM), and 8 mol% yttrium doping in YSZ. (The model used here for LSM is the random model discussed in chapter 4; there is no strain term. Later models did incorporate strain in LSM.) The view is focused on the interface, at a range of only a couple of nanometers. The most salient feature of the result, which is typical for a wide range of potentials and equilibrium constants, is the very tight collection of defects found on the YSZ side of the interface; the concentration profile covers less than a nanometer. This is not particularly surprising, since the Debye length depends inversely on the concentration of mobile defects and the dielectric constant of the material.

5.2.2 A picture of the actual interface

Such a formalism as presented in the previous section might be sufficient to move forward with the blocked electrode experiment and analysis, if we did not have a very clear qualitative picture of the LSM-YSZ interface as provided by TEM and EELS. This work by Backhaus-Ricoult, mentioned above,[5] depicts quite a different picture of the interface than that seen in the results of the model derived in the previous section. Figure 26, taken from ref. [5], depicts cation profiles across the LSM-YSZ interface as determined by EELS. Three things are striking about these results. One, it shows a significant concentration of

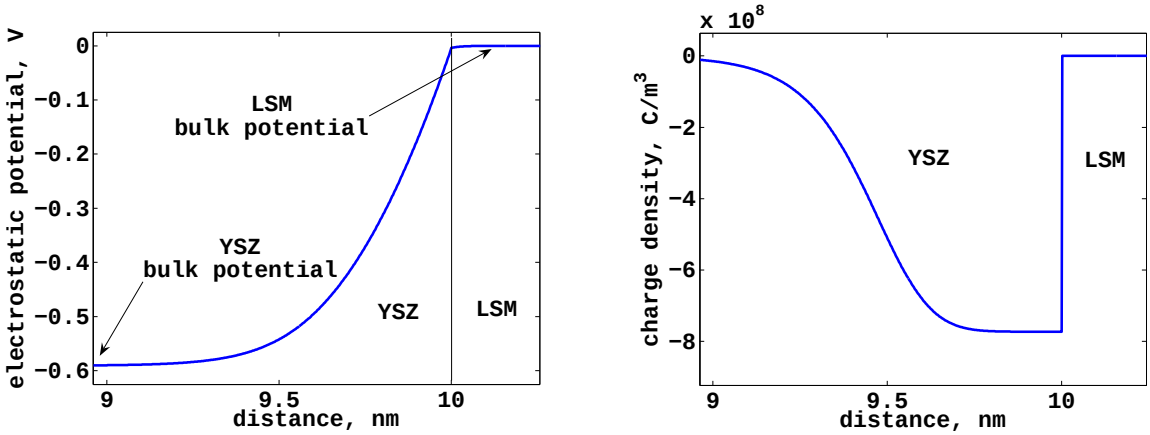

Figure 25: (a) potential and (b) charge density distributions at the YSZ/LSM interface in a blocked electrode under cathodic polarization.

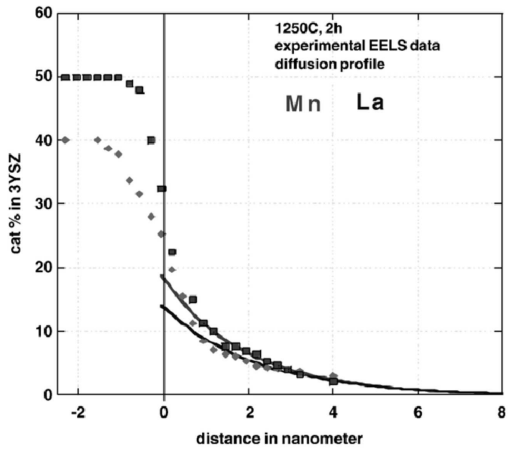

Figure 26: Profiles of La and Mn species near the interface between LSM and YSZ, taken from reference [5]

Mn and La species near the interface in YSZ. Two, the profile extends over several nanometers, as opposed to the profile in Figure 25, which only extends a nanometer or so. Third, and perhaps most important, given that TEM images show no signs of interstitial cations in YSZ or any transitional phase at the boundary, the interface seems, at first glance, to be non-equilibrium: negative defects in LSM (in the form of cation vacancies) share an interface with negative defects in YSZ (substitutional $\mathrm{Mn}'_{\mathrm{Zr}}$, $\mathrm{Mn}''_{\mathrm{Zr}}$ and $\mathrm{La}'_{\mathrm{Zr}}$).

It is, in fact, the opinion of Backhaus-Ricoult that this is a non-equilibrium profile, with metal species partially diffusing into the YSZ structure. While this certainly makes sense from a standpoint of what are likely to be very slow diffusion coefficients for metals

in YSZ, the transport of metal vacancies in LSM should be much faster; there is seemingly no reason for the buildup of cation vacancies on the metal side of the interface, especially with negatively charged dopants opposing it. This suggests clustering of defects on one side of the interface or the other is creating a region of positive charge buildup.

As discussed in chapter 4, the TEM evidence for LSM does not indicate defect clustering. However, the fact that the conductivity decreases with increased aliovalent dopants past the point of approximately 8 mol% Y_2O_3 suggests a clustering of defects in stabilized zirconia, as an attractive interaction between oxygen vacancies and dopant cations. This suggests that a clustering of oxygen vacancies among the negatively-charged substitutional dopants in YSZ could be responsible for the buildup of negatively-charged cation vacancies near the interface in LSM. Additionally, clustering in YSZ may prove to be responsible for the extension of the interface over several nanometers, as opposed to the highly compressed interface seen in Figure 25. In this way, the profile seen in Figure 26 may actually represent an equilibrium or near-equilibrium state.

5.2.3 Cluter variation method in defective ionic solids

The difficulty in writing an equilibrium model for YSZ that considers clusters is the calculation of configurational entropy. One approach to this problem is cluster variation method (CVM). CVM was originally developed as a method of determining phase equilibria in binary alloys, but may be thought of as a general method for calculating configurational entropy for collections of atomic cluster configurations.

The method begins with the selection of a basic configuration of atomic sites in a crystal. Each site is assigned an occupancy operator, which designates the occupancy of the site. Each distinct configuration of this basic figure may be thought of as a distinct cluster. Designation of the fraction of figures in the crystal adhering to each cluster configuration (the cluster variables, x_l) may be thought of as a statistical description of the phase. The task becomes writing the free energy of the crystal in terms of the x_l, then minimizing with respect to them.

Given a pairwise interaction energy between nearest neighbor species (or some higher-order interaction energy), one can easily write the internal energy of the crystal as an appropriate sum over the cluster variables. Writing the entropy in terms of the cluster variables, then, is the key to the method. It is not the purview of this work to present the full derivation of CVM, as several different derivations of the technique appear in the literature.[4, 6, 57, 56, 58, 86, 92] The derivation is carried out with a view to preserving the well-known combinatoric result for the case of completely random distributions of species over the available sites (Fermi-Dirac statistics), and the mathematical certainty of extrapolation to exact results for the case of a basic cluster equal in size to the size of the system. An overview of the basic technique follows.

The entropy of the crystal (per site) can be approximated as:

$$S \approx R \sum_{\eta} \gamma_{\eta} \sum_{l_{\eta}} x_{l_{\eta}} \log x_{l_{\eta}} \tag{43}$$

Here, η denotes certain sub-figures of the basic figure, and l_{η} the distinct configurations (cluster variables) of sub-figure η. The γ_{η} are coefficients, the calculation of which is discussed below. Since all of the cluster variables of a given sub-figure, $x_{l_{\eta'}}$, can be written in terms of cluster variables of the basic figure, x_{l_0} (where the subcript 0 is added here for clarity, and will hereafter denote the cluster variables of the basic figure), equation (43) enables the writing of the free energy per site $\mathfrak{F} = E(x_{l_0}) - TS(x_{l_0})$ in terms of the basic cluster variables.

The appropriate sub-figures to include in the sum (43) are those that can be formed by all overlaps of the basic cluster with itself. The coefficients γ_{η} can then be calculated based upon the number of such figures appearing in the crystal, along with the number of sub-figures appearing in each sub-figure of higher order.

The case of an ionic solid with defects has not been considered up until now to the best of my knowledge, but actually the technique may be applied as discussed above for an ionic solid (having two interpenetrating and mutually exclusive sublattices) so long as the chosen figure adheres to two conditions. These are, that the ratio of sites in the crystal must be preserved in the basic figure, and all sites comprising the basic figure must have

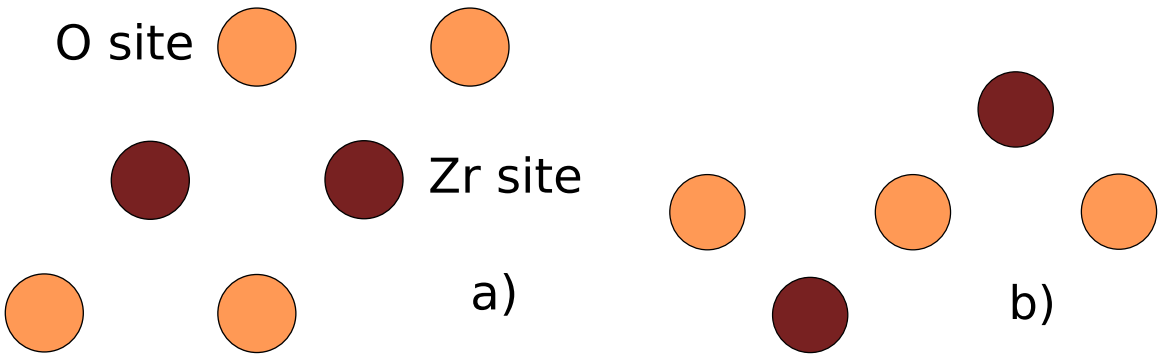

Figure 27: Schematic of the basic figure used with CVM. a) view of cluster orientation with respect to the fluorite (110) b) view with respect to the fluorite (001).

an identical environment within the figure. These requirements preserve the principle that the method becomes exact when the basic figure increases its size to that of the system.[86] The first provision is simple to enforce in the selection of the basic figure. The second can be difficult to accomplish in basic figure selection, but may also be enforced as a constraint on the minimization.

The other constraints on the minimization are normalization ($\sum_l x_{l_0} = 1$) and, for the case of the bulk ionic solid, electroneutrality. The method for constrained minimization is Lagrange multipliers, and for solution Newton's method combined with a so-called natural iteration method (NIM), as introduced by Kikuchi.[57]

The basic figure chosen for the initial analysis of defect clustering in YSZ appears in Figure 27. It was chosen for its relative symmetry and low number of sites (there are only 34 unique cluster variables for the system with only one cation defect). In addition, there are several cation-anion relationships of interest: first and second-nearest neighbors, both of which have attractive bond energies. Solution of the problem using CVM for this figure, with all bonding energies equal to zero produced the random distrbution of defects, as expected.

The method employed for finding bond energies is density functional theory (DFT) calculations, which are quantum-mechanical simulations. The DFT calculations themselves have been performed by Dr. Jeng-Han Wang (now a professor at National Chiao Tung University, Department of Applied Chemistry, Hsinchu, Taiwan). The specific methodology

Table 5: Bond energies for various defect pairs in YSZ

defect pair	**energy, eV**
$(\text{Y-Y})_{1NN}$	0.5551
$(\text{Y-V})_{1NN}$	-0.7392
$(\text{Y-V})_{2NN}$	-0.3516
$(\text{V-V})_{1NN}$	0.8671
$(\text{V-V})_{2NN}$	0.7325

utilizes a simulation space consisting of eight unit cells. Neutral combinations of defects are dispersed in the collection at random. The energy of the ensemble is then calculated using DFT. When a number of cells have been constructed and their energies calculated, a least-squares problem can be solved for the bond energies. Bond energies calculated in this manner for yttrium and oxygen defects appear in Table 5.

Minimizations utilizing these bond energies and the cluster appearing in Figure 27 converged at a wide range of temperatures (300-1000K) and doping fractions (0.0628 - 0.504 mol% yttrium). Evidence of a slight phase changes can be seen at 0.28 mol% between 700 and 800K. An attempt to correlate the cluster information with measured activation energies[39] for conduction in YSZ was unsuccessful. In this effort, we used outside DFT estimates of migration enthalpies for vacancies moving through cation-cation edges of various characters (either Zr-Zr, Zr-Y or Y-Y).[62] Our lack of success here is evidence that ionic conductivity for vacancies cannot be fully described by the energy required to traverse cation-cation edges. DFT-Monte Carlo simulations considering a broader environment when calculating migration enthalpies have had more success in replicating measured activation energy data.[87] Imitating (and perhaps improving upon) these results might be possible using a larger basic figure. However, since the smaller figure may still be suitable for the purposes of accounting for the effects of clustering on the equilibrium structure of the interface, this avenue of study was not pursued further at this time.

5.2.4 Extending CVM for interface studies

In order to extend the CVM technique to the study of the interface, we must apply CVM to a free energy minimization over an entire one-dimensional material domain. This means

that $x_{l_0} = x_{l_0}(\xi)$, and the free energy $\mathfrak{F} = E(x_{l_0}) - TS(x_{l_0}) + (\phi - \phi_0)\rho(x_{l_0})$ (re-written to include electrical energy) becomes a functional over the domain, which we will restrict for the purposes of initial derivation to the YSZ domain, $\xi \in [0, L]$, with metal electrodes (blocking at one side and porous at the other). The free energy functional is:

$$\Phi = \int_0^L \mathfrak{F} d\xi \tag{44}$$

To minimize Φ, we use constrained calculus of variations. The constraints in this case are of two types, pointwise constraints and domain constraints. The pointwise constraints are the normalization condition, the equality of sites condition, and Poisson's equation. The domain constraint is the limitation of the total number of defects, such that the average concentration is equal to the doping fraction. The Lagrange multipliers for the pointwise constraints are also functions of ξ, and as such the pointwise constratins can simply be added to the integrand in equation (44). The domain constraint has a scalar multiplier, and takes an integral form over the domain. The functional becomes:

$$\Phi = \int_0^L \left[\mathfrak{F} + {}^{n}\lambda(1 - \sum_l x_{l_0}) + {}^{o}\lambda \sum_l \nu_l x_{l_0} + {}^{\phi}\lambda \left(\frac{d^2\phi}{d\xi^2} + \frac{\sum_l \rho_l x_{l_0}}{\kappa\epsilon_0} \right) - {}^{y}\lambda \frac{1}{L} \sum_l y_l x_{l_0} \right] d\xi + {}^{y}\lambda f \tag{45}$$

where the ν_l are the relevant coefficients for the site equality constraint, y_l are the coefficients for calculating the concentration of yttrium at a given point, ρ_l are the coefficients for calculating the charge density at a given point and f is the doping fraction.

The method of calculus of variations is to set the first-order variation of the functional for each minimizing function equal to zero. The first-order variation for the cluster variable x_ω is:

$$\frac{\partial \Phi}{\partial x_\omega} \delta x_\omega = \int_0^L \delta x_\omega \left(\frac{\partial \mathfrak{F}}{\partial x_\omega} - {}^{n}\lambda + {}^{o}\lambda \nu_\omega + {}^{\phi}\lambda \frac{\rho_\omega}{\kappa\epsilon_0} - {}^{y}\lambda \frac{y_\omega}{L} \right) d\xi = 0 \tag{46}$$

For the entire expression to be zero for every variation δx_ω, the integrand must be zero. This leads to a set of algebraic equations relating the functions x_{l_0} to the lagrange multipliers and ϕ.

Similarly, for ϕ,

$$\frac{\partial \Phi}{\partial \phi} \delta\phi = \int_0^L \left(\frac{\partial \mathfrak{F}}{\partial \phi} \delta\phi + {}^{\phi}\lambda \delta\phi'' \right) d\xi = 0 \tag{47}$$

Here, the second term in the integrand is integrated by parts twice in order to transfer the derivatives to ${}^{\phi}\lambda$. The boundary terms generated along the way are zero, due to the requirements that the variational term, $\delta\phi$, as well as the Lagrange multiplier ${}^{\phi}\lambda$, are zero at the boundaries. This leads to

$$\frac{\partial \Phi}{\partial \phi}\delta\phi = \int_0^L \delta\phi \left(\frac{\partial \mathfrak{F}}{\partial \phi} + {}^{\phi}\lambda'' \right) d\xi = 0 \tag{48}$$

which again requires that the integrand be zero.

A similar procedure involving variations of the pointwise boundary conditions yields equations setting these conditions identically equal to zero. Since the multiplier ${}^{y}\lambda$ is a constant, no variational argument is necessary; we are simply left with the integral constraint as a final equation.

The reference potential, ϕ_0, does not require a separate Lagrange multiplier, since it can be calculated separately as an analysis of the condition at the boundary. At the porous electrode boundary, we require equilibrium for the reaction

$$\frac{1}{2}\mathsf{O}_2 + \mathsf{V}_{\mathsf{O}}^{\cdot\cdot} + 2e' \leftrightharpoons \mathsf{O}_{\mathsf{O}}^{\mathsf{x}} \tag{49}$$

which leads to the equilibrium condition:

$$\frac{1}{2}\mu_{\mathsf{O}_2} + \mu_{\mathsf{v}}(\xi = 0) + 2\mu_e = 0 \tag{50}$$

where potential-dependent terms in the electrochemical potential have canceled each other out. The electrochemical potential of vacancies at equilibrium is uniform, meaning that the chemical potential at the electrode can be related to that at any reference point. We choose the point (which needs not be actually present in the domain) at which the solid is electrically neutral:

$$\mu_{\mathsf{v}}(\xi = 0) = \mu_{\mathsf{v},0} + 2F\left[\phi_0 - \phi(\xi = 0)\right] \tag{51}$$

Combining equations (49), (50) and (51), and setting $\phi(0) = 0$ yields:

$$\phi_0 = -\frac{1}{2F}\left(\frac{1}{2}\mu_{\mathsf{O}_2} + \mu_{\mathsf{v},0} + 2\mu_e \right) \tag{52}$$

The first and last terms on the right-hand side of equation (52) are constants that can be calculated based on the identity of the metal used in the electrode and the partial pressure

of oxygen. The middle term, $\mu_{\mathsf{v},0}$, which is the chemical potential of vacancies in the neutral solid, is also well-defined, and can be calculated by running the zero-dimensional CVM with enforced vacancy concentrations, using finite difference to calculate the change in the free energy with respect to changes in vacancy concentrations at the point of electroneutrality for the given overall doping fraction.

The system (46)-(48), along with the constraints, is an algebraic-integral-differential set of equations on the domain $\xi \in [0, L]$. It can be solved by discretizing the differential equations – each elliptic, according to the finite element method of equation (41), with, in the case of a known potential drop across the domain, Dirichlet boundary conditions. The FEM, again in this case, allows for easy implementation of adaptive meshing.

In the case of Dirichlet conditions, it is not necessary to include the endpoints of the simulation in the discretization of the algebraic part, equation (46). This is because there is no interdependence between the equations involving $x_{l_0}(0)$ and $x_{l_0}(L)$ and the rest of the equations in the simulation. In fact, in order to solve for these two sets of variables, additional constraints must be employed, equating the electrochemical potentials at those boundaries with the electrochemical potential at the electrically neutral composition.

Implementation of the solution is still in progress.

CHAPTER VI

CONCLUSION

A program of study for quantitative study of oxygen reduction on LSM has been established. The principal parts of the program are carefully designed test cells, which reduce the complexity of the process, the modeling appropriate for those cells, and robust inverse problem techniques that connect the two. Progress in the program of study completed as work for this thesis includes:

1. detailed modeling of oxygen-surface reactions for mixed conductors
2. design and fabrication of patterned films and electrodes of LSM on YSZ (as part of a collaboration)
3. development of detailed electrochemical models for thin films and patterned electrodes, along with their implementation and solution
4. development and implementation of optimization and identification methods
5. proposal of a new theory for bulk defect equilibrium in LSM, along with the testing of that theory against nonstoichiometry data
6. proposal of a new theory to explain the observed structure of the LSM/YSZ interface, along with the design of an experiment to test the theory and the partial development of a quantitative model

The formalism for oxygen reduction on the surface of mixed conductors is unique in that it adheres to a classical theoretical edifice that has been well-studied, in showing that the surface potential does affect the rate of reactions at the MIEC-air interface. This reduces to purely chemical control in certain situations, but charged intermediates may also affect the rate of surface reactions by altering the surface dipole.

The modeling work associated with patterned electrodes is unique for its incorporation of the detailed formalism for oxygen reduction presented in chapter 2, as well as its treatment of sheet resistance. The behavior of the models compare reasonably with experiments performed on thin films and patterned electrodes.

The new model for defects in LSM seems to replicate both nonstoichiometry data, especially at low temperatures, and conductivity data better than its predecessors, even while reducing the ratio of parameters to data points through the simultaneous fitting of the model to multiple temperatures.

The proposal of an equilibrium structure influenced by clustering in YSZ at the boundary with LSM is still in development. The theoretical methodology proposed is a unique expansion of cluster variation method.

I am very hopeful and confident that the program begun in the work for this thesis will continue, producing quantitative knowledge about LSM in the short term that can be used in the optimization of microstructure. I also hope that in the long term a viable methodology for the study of many different types of electrodes has been established.

REFERENCES

[1] Adler, S. B., "Factors governing oxygen reduction in solid oxide fuel cell cathodes," *Chemical Reviews*, vol. 104, no. 10, pp. 4791–4843, 2004.

[2] Adler, S. B., Lane, J. A., and Steele, B. C. H., "Electrode kinetics of porous mixed-conducting oxygen electrodes," *Journal of the Electrochemical Society*, vol. 143, no. 11, pp. 3554–3564, 1996.

[3] Adler, S. B., Lane, J. A., and Steele, B. C. H., "Fundamental issues in modeling of mixed-conductors (a rebuttal to comments on "electrode kinetics of porous mixed-conducting oxygen electrodes")," *Journal of the Electrochemical Society*, vol. 144, no. 5, pp. 1884–1890, 1997.

[4] An, G. Z., "A note on the cluster variation method," *Journal of Statistical Physics*, vol. 52, pp. 727–734, Aug. 1988.

[5] Backhaus-Ricoult, M., "Interface chemistry in LSM-YSZ composite SOFC cathodes," *Solid State Ionics*, vol. 177, pp. 2195–2200, Oct. 2006.

[6] Barker, J. A., "Methods of approximation in the theory of regular mixtures," *Proceedings of the Royal Society of London Series A-Mathematical and Physical Sciences*, vol. 216, no. 1124, pp. 45–56, 1953.

[7] Baumann, F. S., Fleig, J., Habermeier, H. U., and Maier, J., "Impedance spectroscopic study on well-defined $(La,Sr)(Co,Fe)O_{3-\delta}$ model electrodes," *Solid State Ionics*, vol. 177, pp. 1071–1081, Apr. 2006.

[8] Bisquert, J., Gratzel, M., Wang, Q., and Fabregat-Santiago, F., "Three-channel transmission line impedance model for mesoscopic oxide electrodes functionalized with a conductive coating," *Journal of Physical Chemistry B*, vol. 110, pp. 11284–11290, June 2006.

[9] Bockris, J. O., Reddy, A. K. N., and Gamboa-Aldeco, M., *Modern Electrochemistry 2A: Fundamentals of Electrodics*, vol. 2A of *Modern Electrochemistry*. New York: KluwerAcademic / Plenum Publishers, 2nd ed., 1998.

[10] Bouwmeester, H. J. M., Den Otter, M. W., and Boukamp, B. A., "Oxygen transport in $La_{0.6}Sr_{0.4}Co_{1-y}Fe_yO_{3-\delta}$," *Journal of Solid State Electrochemistry*, vol. 8, no. 9, pp. 599–605, 2004.

[11] Brichzin, V., Fleig, J., Habermeier, H. U., Cristiani, G., and Maier, J., "The geometry dependence of the polarization resistance of Sr-doped $LaMnO_3$ microelectrodes on yttria-stabilized zirconia," *Solid State Ionics*, vol. 152, pp. 499–507, 2002.

[12] Brichzin, V., Fleig, J., Habermeier, H. U., and Maier, J., "Geometry dependence of cathode polarization in solid oxide fuel cells investigated by defined Sr-doped $LaMnO_3$ microelectrodes," *Electrochemical and Solid State Letters*, vol. 3, no. 9, pp. 403–406, 2000.

[13] Brumleve, T. R. and Buck, R. P., "Numerical-solution of nernst-planck and poisson equation system with applications to membrane electrochemistry and solid-state physics," *Journal of Electroanalytical Chemistry*, vol. 90, no. 1, pp. 1–31, 1978.

[14] Brumleve, T. R. and Buck, R. P., "Transmission-line equivalent-circuit models for electrochemical impedances," *Journal of Electroanalytical Chemistry*, vol. 126, no. 1-3, pp. 73–104, 1981.

[15] Carnes, B. and Djilali, N., "Systematic parameter estimation for pem fuel cell models," *Journal of Power Sources*, vol. 144, no. 1, pp. 83–93, 2005.

[16] Chebotin, V. N., Remez, I. D., Solovieva, L. M., and Karpachev, S. V., "Electrical double layer in solid electrolytes – theory: oxide electrolytes," *Electrochimica Acta*, vol. 29, no. 10, pp. 1381–1388, 1984.

[17] Choi, Y. M., Wang, J. H., Mebane, D. S., and Liu, M. L., "Oxygen reduction mechanism at the cathode in solid oxide fuel cells," *Catalysis Today*, in press.

[18] Clerc, M. and Kennedy, J., "The particle swarm – explosion, stability, and convergence in a multidimensional complex space," *IEEE Transactions on Evolutionary Computing*, vol. 6, no. 1, pp. 58–73, 2002.

[19] Coffey, G. W., Pederson, L. R., and Rieke, P. C., "Competition between bulk and surface pathways in mixed ionic electronic conducting oxygen electrodes," *Journal of the Electrochemical Society*, vol. 150, no. 8, pp. A1139–A1151, 2003.

[20] De Souza, R. A. and Kilner, J. A., "Oxygen transport in $La_{1-x}Sr_xMn_{1-y}Co_yO_{3\pm\delta}$ perovskites, Part I. Oxygen tracer diffusion," *Solid State Ionics*, vol. 106, no. 3-4, pp. 175–187, 1998.

[21] De Souza, R. A. and Kilner, J. A., "Oxygen transport in $La_{1-x}Sr_xMn_{1-y}Co_yO_{3\pm\delta}$ perovskites, Part II. Oxygen surface exchange," *Solid State Ionics*, vol. 126, no. 1-2, pp. 153–161, 1999.

[22] De Souza, R. A., Kilner, J. A., and Walker, J. F., "A SIMS study of oxygen tracer diffusion and surface exchange in $La_{0.8}Sr_{0.2}MnO_{3\pm\delta}$," *Materials Letters*, vol. 43, no. 1-2, pp. 43–52, 2000.

[23] Delahay, P., *Double Layer and Electrode Kinetics*. New York: Interscience, 1965.

[24] Deseure, J., Bultel, Y., Dessemond, L., and Siebert, E., "Modelling of DC and AC responses of a planar mixed conducting oxygen electrode," *Solid State Ionics*, vol. 176, pp. 235–244, 2005.

[25] Deseure, J., Bultel, Y., Dessemond, L., and Siebert, E., "Theoretical optimisation of a SOFC composite cathode," *Electrochimica Acta*, vol. 50, no. 10, pp. 2037–2046, 2005.

[26] Endo, A., Fukunaga, H., Wen, C., and Yamada, K., "Cathodic reaction mechanism of dense $La_{0.6}Sr_{0.4}CoO_3$ and $La_{0.81}Sr_{0.09}MnO_3$ electrodes for solid oxide fuel cells," *Solid State Ionics*, vol. 135, no. 1-4, pp. 353–358, 2000.

[27] Endo, A., Ihara, M., Komiyama, H., and Yamada, K., "Cathodic reaction mechanism for dense Sr-doped lanthanum manganite electrodes," *Solid State Ionics*, vol. 86-8, pp. 1191–1195, 1996.

[28] Endo, A., Wada, S., Wen, C. J., Komiyama, H., and Yamada, K., "Low overvoltage mechanism of high ionic conducting cathode for solid oxide fuel cell," *Journal of the Electrochemical Society*, vol. 145, no. 3, pp. L35–L37, 1998.

[29] Erdey-Grúz, T., *Kinetics of Electrode Processes*. Budapest: Wiley-Interscience, 1972.

[30] Evitts, R. W., *Modelling of Crevice Corrosion*. PhD thesis, University of Saskatchewan, 1997.

[31] Fleig, J., "On the width of the electrochemically active region in mixed conducting solid oxide fuel cell cathodes," *Journal of Power Sources*, vol. 105, no. 2, pp. 228–238, 2002.

[32] Fleig, J., "Solid oxide fuel cell cathodes: Polarization mechanisms and modeling of the electrochemical performance," *Annual Review of Materials Research*, vol. 33, pp. 361–382, 2003.

[33] Fleig, J., "On the current-voltage characteristics of charge transfer reactions at mixed conducting electrodes on solid electrolytes," *Physical Chemistry Chemical Physics*, vol. 7, no. 9, pp. 2027–2037, 2005.

[34] Fleig, J. and Jamnik, J., "Work function changes of polarized electrodes on solid electrolytes," *Journal of the Electrochemical Society*, vol. 152, no. 4, pp. E138–E145, 2005.

[35] Fleig, J. and Maier, J., "The polarization of mixed conducting SOFC cathodes: Effects of surface reaction coefficient, ionic conductivity and geometry," *Journal of the European Ceramic Society*, vol. 24, no. 6, pp. 1343–1347, 2004.

[36] Fleig, J., Pham, P., Sztulzaft, P., and Maier, J., "Inhomogeneous current distributions at grain boundaries and electrodes and their impact on the impedance," *Solid State Ionics*, vol. 115, pp. 739–747, 1998.

[37] Giles, M. B. and Pierce, N. A., "An introduction to the adjoint approach to design," *Flow, Turbulence and Combustion*, vol. 65, pp. 393–415, 2000.

[38] Grundy, A. N., Hallstedt, B., and Gauckler, L. J., "Assessment of the $La - Sr - Mn - O$ system," *CALPHAD*, vol. 28, no. 2, pp. 191–201, 2004.

[39] Hartmanova, M., Schneider, J., Navratil, V., Kundracik, F., Schulz, H., and Lomonova, E. E., "Correlation between microscopic and macroscopic properties of yttria stabilized zirconia 1. single crystals," *Solid State Ionics*, vol. 136, pp. 107–113, Nov. 2000.

[40] Hendriks, M. G. H. M., tenElshof, J. E., Bouwmeester, H. J. M., and Verweij, H., "The electrochemical double-layer capacitance of yttria-stabilised zirconia," *Solid State Ionics*, vol. 146, pp. 211–217, 2002.

[41] Herbstritt, D., Weber, A., and Ivers-Tiffee, E., "Modelling and DC-polarisation of a three dimensional electrode/electrolyte interface," *Journal of the European Ceramic Society*, vol. 21, no. 10-11, pp. 1813–1816, 2001.

[42] Horita, T., Yamaji, K., Ishikawa, M., Sakai, N., Yokokawa, H., Kawada, T., and Kato, T., "Active sites imaging for oxygen reduction at the $La_{0.9}Sr_{0.1}MnO_{3-x}$/yttria-stabilized zirconia interface by secondary-ion mass spectrometry," *Journal of the Electrochemical Society*, vol. 145, no. 9, pp. 3196–3202, 1998.

[43] Huang, K. Q. and Goodenough, J. B., "Oxygen permeation through cobalt-containing perovskites – surface oxygen exchange vs. lattice oxygen diffusion," *Journal of the Electrochemical Society*, vol. 148, no. 5, pp. E203–E214, 2001.

[44] Imanishi, N., Matsumura, T., Sumiya, Y., Yoshimura, K., Hirano, A., Takeda, Y., Mori, D., and Kanno, R., "Impedance spectroscopy of perovskite air electrodes for SOFC prepared by laser ablation method," *Solid State Ionics*, vol. 174, pp. 245–252, Oct. 2004.

[45] Ioroi, T., Hara, T., Uchimoto, Y., Ogumi, Z., and Takehara, Z., "Preparation of perovskite-type $La_{1-x}Sr_xMnO_3$ films by vapor-phase processes and their electrochemical properties," *Journal of the Electrochemical Society*, vol. 144, no. 4, pp. 1362–1370, 1997.

[46] Ioroi, T., Hara, T., Uchimoto, Y., Ogumi, Z., and Takehara, Z., "Preparation of perovskite-type $La_{1-x}Sr_xMnO_3$ films by vapor-phase processes and their electrochemical properties, II. Effects of doping strontium to $LaMnO_3$ on the electrode properties," *Journal of the Electrochemical Society*, vol. 145, pp. 1999–2004, June 1998.

[47] Jamnik, J. and Maier, J., "Generalised equivalent circuits for mass and charge transport: chemical capacitance and its implications," *Physical Chemistry Chemical Physics*, vol. 3, no. 9, pp. 1668–1678, 2001.

[48] Jiang, S. P. and Love, J. G., "Origin of the initial polarization behavior of Sr-doped $LaMnO_3$ for O_2 reduction in solid oxide fuel cells," *Solid State Ionics*, vol. 138, pp. 183–190, 2001.

[49] Jiang, S. P. and Love, J. G., "Observation of structural change induced by cathodic polarization on $(La, Sr)MnO_3$ electrodes of solid oxide fuel cells," *Solid State Ionics*, vol. 158, no. 1-2, pp. 45–53, 2003.

[50] Jiang, Y., Wang, S. Z., Zhang, Y. H., Yan, J. W., and Li, W. Z., "Kinetic study of the formation of oxygen vacancy on lanthanum manganite electrodes," *Journal of the Electrochemical Society*, vol. 145, no. 2, pp. 373–378, 1998.

[51] Kamata, H., Yonemura, Y., Mizusaki, J., Tagawa, H., Naraya, K., and Sasamoto, T., "High-temperature electrical-properties of the perovskite-type oxide $La_{1-x}Sr_xMnO_{3-\delta}$," *Journal of Physics and Chemistry of Solids*, vol. 56, no. 7, pp. 943–950, 1995.

[52] Kamata, K., Nakajima, T., Hayashi, T., and Nakamura, T., "Nonstoichiometric behavior and phase-stability of rare-earth manganites at 1200-degrees-c .1. lamno3," *Materials Research Bulletin*, vol. 13, no. 1, pp. 49–54, 1978.

[53] Kawada, T., Masuda, K., Suzuki, J., Kaimai, A., Kawamura, K., Nigara, Y., Mizusaki, J., Yugami, H., Arashi, H., Sakai, N., and Yokokawa, H., "Oxygen isotope exchange with a dense $La_{0.6}Sr_{0.4}CoO_{3-\delta}$ electrode on a $Ce_{0.9}Ca_{0.1}O_{1.9}$ electrolyte," *Solid State Ionics*, vol. 121, no. 1-4, pp. 271–279, 1999.

[54] Kawada, T., Suzuki, J., Sase, M., Kaimai, A., Yashiro, K., Nigara, Y., Mizusaki, J., Kawamura, K., and Yugami, H., "Determination of oxygen vacancy concentration in a thin film of $La_{0.6}Sr_{0.4}CoO_{3-\delta}$ by an electrochemical method," *Journal of the Electrochemical Society*, vol. 149, no. 7, pp. E252–E259, 2002.

[55] Kennedy, J. and Eberhardt, R. C., "Particle swarm optimization," in *Proceedings of the IEEE International Conference in Neural Networks*, (Perth, Australia), p. 1942, 1995.

[56] Kikuchi, R., "A theory of cooperative phenomena," *Physical Review*, vol. 81, no. 6, pp. 988–1003, 1951.

[57] Kikuchi, R., "Superposition approximation and natural iteration calculation in cluster-variation method," *Journal of Chemical Physics*, vol. 60, no. 3, pp. 1071–1080, 1974.

[58] Kikuchi, R. and Brush, S. G., "Improvement of cluster-variation method," *Journal of Chemical Physics*, vol. 47, no. 1, pp. 195–&, 1967.

[59] Kilner, J. A., DeSouza, R. A., and Fullarton, I. C., "Surface exchange of oxygen in mixed conducting perovskite oxides," *Solid State Ionics*, vol. 86-8, pp. 703–709, 1996.

[60] Koep, E., Compson, C., Liu, M. L., and Zhou, Z. P., "A photolithographic process for investigation of electrode reaction sites in solid oxide fuel cells," *Solid State Ionics*, vol. 176, no. 1-2, pp. 1–8, 2005.

[61] Koep, E., Mebane, D. S., Das, R., Compson, C., and Liu, M. L., "The characteristic thickness for a dense $La_{0.8}Sr_{0.2}MnO_3$ electrode," *Electrochemical and Solid State Letters*, vol. 8, no. 11, pp. A592–A595, 2005.

[62] Krishnamurthy, R., Yoon, Y. G., Srolovitz, D. J. and Car, R., "Oxygen diffusion in yttria-stabilized zirconia: A new simulation model," *Journal of the American Ceramic Society*, vol. 87, pp. 1821–1830, Oct. 2004.

[63] Kuo, J. H. and Anderson, H. U., "Oxidation-reduction behavior of undoped and Sr-doped $LaMnO_3$: Defect structure, electrical conductivity, and thermoelectric power," *Journal of Solid State Chemistry*, vol. 87, pp. 55–63, 1990.

[64] Kuo, J. H., Anderson, H. U., and Sparlin, D. M., "Oxidation-reduction behavior of undoped and Sr-doped $LaMnO_3$ nonstoichiometry and defect structure," *Journal of Solid State Chemistry*, vol. 83, no. 1, pp. 52–60, 1989.

[65] Kuznecov, M., Otschik, P., Trofimenko, N., and Eichler, K., "Oxygen transport in the SOFC cathode," *Russian Journal of Electrochemistry*, vol. 40, no. 11, pp. 1162–1169, 2004.

[66] Lane, J. A., Benson, S. J., Waller, D., and Kilner, J. A., "Oxygen transport in $La_{0.6}Sr_{0.4}Co_{0.2}Fe_{0.8}O_{3-\delta}$," *Solid State Ionics*, vol. 121, no. 1-4, pp. 201–208, 1999.

[67] Lane, J. A. and Kilner, J. A., "Measuring oxygen diffusion and oxygen surface exchange by conductivity relaxation," *Solid State Ionics*, vol. 136, pp. 997–1001, 2000.

[68] Larché, F. C. and Cahn, J. W., "The effect of self-stress on diffusion in solids," *Acta Metall.*, vol. 30, no. 10, pp. 1835–1845, 1982.

[69] Lauret, H. and Hammou, A., "Localization of oxygen cathodic reduction zone at lanthanum manganite zirconia interface," *Journal of the European Ceramic Society*, vol. 16, no. 4, pp. 447–451, 1996.

[70] Liu, M. L. and Winnick, J., "Fundamental issues in modeling of mixed ionic-electronic conductors (MIECs)," *Solid State Ionics*, vol. 118, no. 1-2, pp. 11–21, 1999.

[71] Mamak, M., Metraux, G. S., Petrov, S., Coombs, N., Ozin, G. A., and Green, M. A., "Lanthanum strontium manganite/yttria-stabilized zirconia nanocomposites derived from a surfactant assisted, co-assembled mesoporous phase," *Journal of the American Chemical Society*, vol. 125, pp. 5161–5175, 2003.

[72] McEvoy, A. J., "Materials for high-temperature oxygen reduction in solid oxide fuel cells," *Journal of Materials Science*, vol. 36, no. 5, pp. 1087–1091, 2001.

[73] Mendes, R., Kennedy, J., and Neves, J., "The fully informed particle swarm: Simpler, maybe better," *IEEE Transactions on Evolutionary Computing*, vol. 8, pp. 204–210, June 2004.

[74] Mims, C. A., Joos, N. I., van der Heide, P. A. W., Jacobson, A. J., Chen, C., Chu, C. W., Kim, B. I., and Perry, S. S., "Oxygen transport in oxide thin film structures oriented $La_{0.5}Sr_{0.5}CoO_{3-x}$ on single-crystal yttria-stabilized zirconia," *Electrochemical and Solid State Letters*, vol. 3, pp. 59–61, Jan. 2000.

[75] Minh, N. Q. and Takahashi, T., *Science and Technology of Ceramic Fuel Cells*. Amsterdam, New York: Elsevier Science, 1995.

[76] Mizusaki, J., Mori, N., Takai, H., Yonemura, Y., Minamiue, H., Tagawa, H., Dokiya, M., Inaba, H., Naraya, K., Sasamoto, T., and Hashimoto, T., "Oxygen nonstoichiometry and defect equilibrium in the perovskite-type oxides $La_{1-x}Sr_xMnO_{3+\delta}$," *Solid State Ionics*, vol. 129, no. 1-4, pp. 163–177, 2000.

[77] Mizusaki, J., Saito, T., and Tagawa, H., "A chemical diffusion-controlled electrode reaction at the compact $La_{1-x}Sr_xMnO_3$/stabilized zirconia interface in oxygen atmospheres," *Journal of the Electrochemical Society*, vol. 143, no. 10, pp. 3065–3073, 1996.

[78] Mizusaki, J., Tagawa, H., Naraya, K., and Sasamoto, T., "Nonstoichiometry and thermochemical stability of the perovskite-type $La_{1-x}Sr_xMnO_{3-\sigma}$," *Solid State Ionics*, vol. 49, pp. 111–118, Dec. 1991.

[79] Mizusaki, J., Yonemura, Y., Kamata, H., Ohyama, K., Mori, N., Takai, H., Tagawa, H., Dokiya, M., Naraya, K., Sasamoto, T., Inaba, H., and Hashimoto, T., "Electronic conductivity, seebeck coefficient, defect and electronic structure of nonstoichiometric $La_{1-x}Sr_xMnO_3$," *Solid State Ionics*, vol. 132, no. 3-4, pp. 167–180, 2000.

[80] Mori, D., Oka, H., Suzuki, Y., Sonoyama, N., Yamada, A., Kanno, R., Sumiya, Y., Imanishi, N., and Takeda, Y., "Synthesis, structure, and electrochemical properties of epitaxial perovskite $La_{0.8}Sr_{0.2}CoO_3$ film on ysz substrate," *Solid State Ionics*, vol. 177, pp. 535–540, Feb. 2006.

[81] Newman, J. and Thomas-Alyea, K. E., *Electrochemical Systems*. Hoboken, NJ: Wiley-Interscience, 3rd ed., 2004.

[82] Nowotny, J. and Rekas, M., "Defect chemistry of $(La, Sr)MnO_3$," *Journal of the American Ceramic Society*, vol. 81, no. 1, pp. 67–80, 1998.

[83] Ormerod, R. M., "Solid oxide fuel cells," *Chemical Society Reviews*, vol. 32, no. 1, pp. 17–28, 2003.

[84] Parsons, R., "General equations for the kinetics of electrode processes," *Transactions of The Faraday Society*, vol. 47, no. 12, pp. 1332–1344, 1951.

[85] Patankar, S., *Numerical Heat Transfer and Fluid Flow*. New York: Hemisphere Publishing Corp., 1980.

[86] Pelizzola, A., "Cluster variation method in statistical physics and probabilistic graphical models," *Journal of Physics A-Mathematical and General*, vol. 38, pp. R309–R339, Aug. 2005.

[87] Pornprasertsuk, R., Ramanarayanan, P., Musgrave, C. B., and Prinz, F. B., "Predicting ionic conductivity of solid oxide fuel cell electrolyte from first principles," *Journal of Applied Physics*, vol. 98, p. 103513, Nov. 2005.

[88] Poulsen, F. W., "Defect chemistry modelling of oxygen-stoichiometry, vacancy concentrations, and conductivity of $(La_{1-x}Sr_x)_yMnO_{3\pm\delta}$," *Solid State Ionics*, vol. 129, no. 1-4, pp. 145–162, 2000.

[89] Princivalle, A., Perednis, D., Neagu, R., and Djurado, E., "Microstructural investigations of nanostructured $La(Sr)MnO_{3-\delta}$ films deposited by electrostatic spray deposition," *Chemistry of Materials*, vol. 16, pp. 3733–3739, 2004.

[90] Riess, I., "Recent investigations into the properties of mixed ionic electronic conductors," *Materials Science and Engineering B-Solid State Materials for Advanced Technology*, vol. 12, pp. 351–356, Feb. 1992.

[91] Ringuede, A. and Fouletier, J., "Oxygen reaction on strontium-doped lanthanum cobaltite dense electrodes at intermediate temperatures," *Solid State Ionics*, vol. 139, pp. 167–177, Feb. 2001.

[92] Sanchez, J. M. and Fontaine, D. D., "FCC ising-model in cluster variation approximation," *Physical Review B*, vol. 17, no. 7, pp. 2926–2936, 1978.

[93] Sasaki, K., Wurth, J. P., Gschwend, R., Godickemeier, M., and Gauckler, L. J., "Microstructure-property relations of solid oxide fuel cell cathodes and current collectors - cathodic polarization and ohmic resistance," *Journal of the Electrochemical Society*, vol. 143, no. 2, pp. 530–543, 1996.

[94] Siebert, E., Hammouche, A., and Kleitz, M., "Impedance spectroscopy analysis of $La_{1-x}Sr_xMnO_3$-yttria-stabilized zirconia electrode-kinetics," *Electrochimica Acta*, vol. 40, no. 11, pp. 1741–1753, 1995.

[95] Singhal, S. C., "Advances in solid oxide fuel cell technology," *Solid State Ionics*, vol. 135, no. 1-4, pp. 305–313, 2000.

[96] Sunde, S., "Simulations of composite electrodes in fuel cells," *Journal of Electroceramics*, vol. 5, no. 2, pp. 153–182, 2000.

[97] Svensson, A. M., Sunde, S., and Nisancioglu, K., "Mathematical modeling of oxygen exchange and transport in air-perovskite-YSZ interface regions I. Reduction of intermediately adsorbed oxygen," *Journal of the Electrochemical Society*, vol. 144, no. 8, pp. 2719–2732, 1997.

[98] Svensson, A. M., Sunde, S., and Nisancioglu, K., "Mathematical modeling of oxygen exchange and transport in air-perovskite-yttria-stabilized zirconia interface regions II. Direct exchange of oxygen vacancies," *Journal of the Electrochemical Society*, vol. 145, no. 4, pp. 1390–1400, 1998.

[99] Takeda, Y., Kanno, R., Noda, M., Tomida, Y., and Yamamoto, O., "Cathodic polarization phenomena of perovskite oxide electrodes with stabilized zirconia," *Journal of the Electrochemical Society*, vol. 134, no. 11, pp. 2656–2661, 1987.

[100] tenElshof, J. E., Hekdriks, M. G. H. M., Bouwmeester, H. J. M., and Verweij, H., "The near-surface defect structure of yttria-stabilised zirconia determined by measurement of the differential capacity," *Journal of Materials Chemistry*, vol. 11, pp. 2564–2571, 2001.

[101] vanHassel, B. A., Kawada, T., Sakai, N., Yokokawa, H., Dokiya, M., and Bouwmeester, H. J. M., "Oxygen permeation modeling of perovskites," *Solid State Ionics*, vol. 66, pp. 295–305, 1993.

[102] vanHeuveln, F. H. and Bouwmeester, H. J. M., "Electrode properties of Sr-doped $LaMnO_3$ on yttria-stabilized zirconia, 2. Electrode kinetics," *Journal of the Electrochemical Society*, vol. 144, no. 1, pp. 134–140, 1997.

[103] vanRoosmalen, J. A. M. and Cordfunke, E. H. P., "Defect chemistry of $LaMnO_{3\pm\delta}$, 4. Defect model for $LaMnO_{3+\delta}$," *Journal of Solid State Chemistry*, vol. 110, pp. 109–112, 1994.

[104] vanRoosmalen, J. A. M. and Cordfunke, E. H. P., "The defect chemistry of $LaMnO_{3\pm\delta}$, 5. Thermodynamics," *Journal of Solid State Chemistry*, vol. 110, pp. 113–117, May 1994.

[105] vanRoosmalen, J. A. M., Cordfunke, E. H. P., Helmholdt, R. B., and Zandbergen, H. W., "The defect chemistry of $LaMnO_{3\pm\delta}$, 2. Structural aspects of $LaMnO_{3\pm\delta}$," *Journal of Solid State Chemistry*, vol. 110, pp. 100–105, May 1994.

[106] Vayenas, C. G., Brosda, S., and Pliangos, C., "The double-layer approach to promotion, electrocatalysis, electrochemical promotion, and metal-support interactions," *Journal of Catalysis*, vol. 216, no. 1-2, pp. 487–504, 2003.

[107] Wang, W. and Jiang, S. P., "A mechanistic study on the activation process of $(La, Sr)MnO_3$ electrodes of solid oxide fuel cells," *Solid State Ionics*, vol. 177, pp. 1361–1369, 2006.

[108] Wang, W. G., Liu, Y. L., Barfod, R., Schougaard, S. B., Gordes, P., Ramousse, S., Hendriksen, P. V., and Mogensen, M., "Nanostructured lanthanum manganate composite cathode," *Electrochemical and Solid State Letters*, vol. 8, pp. A619–A621, 2005.

[109] Williford, R. E. and Singh, P., "Engineered cathodes for high performance SOFCs," *Journal of Power Sources*, vol. 128, no. 1, pp. 45–53, 2004.

[110] Yang, Y. L., Chen, C. L., Chen, S. Y., Chu, C. W., and Jacobson, A. J., "Impedance studies of oxygen exchange on dense thin film electrodes of $La_{0.5}Sr_{0.5}CoO_{3-\delta}$," *Journal of the Electrochemical Society*, vol. 147, pp. 4001–4007, Nov. 2000.

[111] Yang, Y. M. L., Jacobson, A. J., Chen, C. L., Luo, G. P., Ross, K. D., and Chu, C. W., "Oxygen exchange kinetics on a highly oriented $La_{0.5}Sr_{0.5}CoO_{3-\delta}$ thin film prepared by pulsed-laser deposition," *Applied Physics Letters*, vol. 79, pp. 776–778, Aug. 2001.

[112] Yasumoto, K., Mori, N., Mizusaki, J., Tagawa, H., and Dokiya, M., "Effect of oxygen nonstoichiometry on electrode activity of $La_{(1-x)}A_{(x)}MnO_{(3\pm\delta)}$ cathode," *Journal of the Electrochemical Society*, vol. 148, no. 1, pp. A105–A111, 2001.

[113] Zipprich, W., Waschilewski, S., Rocholl, F., and Wiemhofer, H. D., "Improved preparation of $La_{1-x}Me_xCoO_{3-\delta}(Me = Sr, Ca)$ and analysis of oxide ion conductivity with ion conducting microcontacts," *Solid State Ionics*, vol. 101, pp. 1015–1023, 1997.

[114] Zipprich, W. and Wiemhofer, H. D., "Measurement of ionic conductivity in mixed conducting compounds using solid electrolyte microcontacts," *Solid State Ionics*, vol. 135, no. 1-4, pp. 699–707, 2000.

VITA

Education

Ph.D., Materials Science and Engineering, Georgia Institute of Technology, expected Dec. 2007.

M.S., Materials Science and Engineering, Georgia Institute of Technology, 2004.

B.A., Mechanical Engineering and History, Rice University, 1996.

Publications

1. M. Lynch, D. S. Mebane, Y. Liu, M. L. Liu, "Triple Phase Boundary and Surface Transport in a Numerical Mixed Conducting Thin Film Patterned Electrode Model," *Journal of the Electrochemical Society* (2007) submitted.

2. D. S. Mebane, Y. Liu and M. L. Liu, "Refinement of the Bulk Defect Model for $La_xSr_{1-x}MnO_{3\pm\delta}$," *Solid State Ionics*, (2007) accepted.

3. Y. M. Choi, J. H. Wang, D. S. Mebane and M. L. Liu, "Oxygen Reduction Mechanism at Cathode Materials in Solid Oxide Fuel Cells," (Invited Review) *Catalysis Today*, (2007) in press.

4. Y. M. Choi, D. S. Mebane, M. C. Lin and M. L. Liu, "Oxygen Reduction for $LaMnO_3$-Based Cathode Materials in Solid Oxide Fuel Cells," *Chemistry of Materials*, **19** (2007) 1690.

5. D. S. Mebane, Y. Liu and M. L. Liu, "A Two-Dimensional Model and Numerical Treatment for Mixed Conducting Thin Films," *Journal of the Electrochemical Society*, **154** (2007) A421.

6. D. S. Mebane and M. L. Liu, "Classical, Phenomenological Analysis of the Kinetics of Reactions at the Gas-Exposed Surface of Mixed Ionic Electronic Conductors," *Journal*

of Solid State Electrochemistry, **10** (2006) 575.

7. E. Koep, D. S. Mebane, R. Das, C. Compson and M. L. Liu, "The Characteristic Thickness for a $La_{0.8}Sr_{0.2}MnO_3$ Electrode," *Electrochemical and Solid State Letters*, **8** (2005) A592.

8. D. S. Mebane and R. A. Gerhardt, "Interpreting Impedance Response of Silicon Carbide Whisker / Alumina Composites Through Microstructural Simulation," *Journal of the American Ceramic Society*, **89** (2006) 538.

9. D. S. Mebane, A. M. Gokhale and R. A. Gerhardt, "Trivariate, Stereological Length-Radius-Orientation Unfolding Derived and Applied to Alumina-Silicon Carbide Whisker Composites," *Journal of the American Ceramic Society*, **89** (2006) 620.

10. D. S. Mebane, S. I. Lieberman, A. M. Gokhale and R. A. Gerhardt, "Bivariate Stereological Unfolding Procedure for Randomly Oriented Chopped Fibers or Whiskers," *Acta Materialia*, **53** (2005) 4943.

Professional Presentations

1. D. S. Mebane, Y. Liu and M. L. Liu, "A Low-Temperature Bulk Model for $La_xSr_{1-x}MnO_{3\pm\delta}$," European Ceramic Society Conference, 2007.

2. D. S. Mebane and M. L. Liu, "Modeling of MIEC Cathodes: The Effect of Sheet Resistance," American Ceramic Society Cocoa Beach 2006, in *Advances in Solid Oxide Fuel Cells, Ceramic Transactions*, A. Wereczak and E. Lara-Curzio, Eds., The American Ceramic Society, 2007.

3. D. S. Mebane, A. M. Gokhale and M. L. Liu, "Explicit Computational Investigations on the Effect of Microstructure in Solid Oxide Fuel Cell Electrodes," Microscopy and Microanalysis 2005.

4. D. S. Mebane and R. A. Gerhardt, "Impedance Response of Alumina Silicon Carbide Whisker Composites," TMS 2005.

5. S. I. Lieberman, D. S. Mebane, A. M. Gokhale and R. A. Gerhardt, "First Application of a Novel Stereological Length-Radius Unfolding Procedure to Determine the Three-Dimensional Bivariate Size and Shape Distribution of TiB Whiskers in Ti-6Al-4V-2.9B," TMS 2005.

6. D. S. Mebane, A. M. Gokhale and R. A. Gerhardt, "The Effect of Microstructural Interconnectivity on the Resistivity of Al_2O_3-SiC_w Composites," NUMIFORM 2004, in *Materials Processing and Design: Modeling, Simulation and Applications*, S. Ghoth, J. M. Castro, J. K. Lee, Eds., American Institute of Physics, 2004, p. 350.

Skillset

- Design and C++ imlpementation of numerical methods for partial differential equations and statistical physics
- Parameter estimation/inverse problem methodology, including particle swarm optimization
- Electrochemistry, solid-state physics and thermodynamics with advanced knowledge in mixed ionic-electronic conductors
- Impedance spectroscopy and other electrochemical experiments, SEM, quantitative stereology, optical microscopy, and X-ray diffraction
- Microstructural modeling and statistical analysis of microstructure-property relationships
- Ability to assemble and lead, or work within project teams
- Strong written and oral communication, with grant proposal writing experience

Awards

- NSF International Fellowship, 2008-2010
- NSF International Travel Award, 2007

- Boeing Fellow, 2005-2007
- Best Master's Thesis, School of Materials Science and Engineering, Georgia Tech, 2004

Work History

Executive Recruiter, Leader Institute, Marietta, GA, 2001-2002

Executive Recruiter, Self-employed, New Orleans, LA, 2000-2001

Executive Recruiter, MSI International, New Orleans, LA, 1998-2000

Community Activism

Commissioner-appointed member, DeKalb County Citizens' Homelessness Task Force, 2005-2007

Volunteer, Central Presbyterian Outreach and Advocacy Center, 2003-2007

Volunteer, Decatur Cooperative Ministry, 2004-2007